Solubility and speciation of sulfur in silicate melts under crustal conditions

Lauren R. Gorojovsky, Department of Earth Sciences, University of Oxford
Lauren.gorojovsky@earth.ox.ac.uk
Bernard J. Wood, [a]Department of Earth Sciences, University of Oxford
Bernie.wood@earth.ox.ac.uk

This preprint is not an accepted peer-reviewed manuscript. This manuscript has been submitted to Earth and Planetary Science Letters (EPSL) and is currently under review.

Solubility and speciation of sulfur in silicate melts under crustal conditions

Lauren R. Gorojovsky[a*], Bernard J. Wood[a]

[a]Department of Earth Sciences, University of Oxford, South Parks Road, Oxford, OX1 3AN, UK

* lauren.gorojovsky@earth.ox.ac.uk

Keywords: sulfur; redox; sulfide; magma; subduction; porphyry

Highlights

- Sulfide and sulfate capacities experimentally constrained in silicate melts at 1050 to 1250 °C.
- The change in S^{6+}/S^{2-} of a silicate melt with $\log fO_2$ is strongly temperature dependent < 1200 °C.
- Fe-S redox exchange may oxidise arc magmas by several log units in fO_2 as they crystallise.
- Sulfide saturation is widespread in oxidised (> ΔFMQ +2) calc-alkaline magmas.
- Cu-rich fluids should form by remobilising cumulate sulfides not sulfide-undersaturated melts.

Abstract

We have determined the solubility of sulfur as either sulfide (S^{2-}) or sulfate (S^{6+}) in a wide range of silicate melts at 1 atm pressure and temperatures of 1050° to 1250°C. The method involved suspension of the melt in either a mixture of CO_2-CO-SO_2 (sulfide solubility) or SO_2 and air (sulfate solubility) for periods of up to 120 hours. Sulfur concentrations, measured by electron microprobe were converted into sulfide capacity $C_{S^{2-}}$ and sulfate capacity $C_{S^{6+}}$ using (Fincham and Richardson; 1954):

$$\log C_{S^{2-}} = \log[S^{2-}] + \frac{1}{2}\log\frac{fS_2}{fO_2}$$

$$\log C_{S^{6+}} = \log[SO_4^{2-}] - \frac{1}{2}\log fS_2 - \frac{3}{2}\log fO_2$$

$[S^{2-}]$ and $[SO_4^{2-}]$ refer to weight % sulfur dissolved in the melt as sulfate and sulfide respectively. Our new results demonstrate that extrapolation of earlier data to temperatures below 1200°C yields good

agreement for sulfide capacity but overestimates sulfate capacity. This means that sulfide is appreciably more stable relative to sulfate in crustal magmas (temperatures <1200°C) than previously calculated.

A major consequence is that the crossover from S^{2-} at low fO_2 to S^{6+} at high fO_2 shifts upwards by ~0.6 logfO_2 units relative to the FMQ buffer as temperature declines from 1200° to 1050°C. The large temperature effect on sulfur speciation also means that there is electron exchange between Fe^{2+} and S^{6+} during magma cooling and ascent leading to high measured Fe^{3+}/Fe^{2+} in quenched melts, high calculated fO_2 and relatively reduced sulfur with high S^{2-}/S^{6+}even at +2-3 logfO_2 units above the FMQ buffer. This self-oxidation mechanism at low temperatures is a major contribution to the observation that hydrous S-bearing arc magmas are more oxidised than MORB, which are generated at low fO_2 and which erupt at higher temperatures. Furthermore, these oxidised hydrous melts are sulfide saturated and should precipitate an Fe-rich sulfide throughout their path of ascent and differentiation in lower, mid and upper -crustal levels. Given that such sulfides would scavenge Cu and other chalcophile metals we suggest that the occurrence of Cu-(±Au) porphyry deposits is governed less by the capacity of magmas to remain Cu-rich, and more by the architecture and evolution of the cumulate pile, the timing and depth of volatile saturation, and the efficiency of Cl-rich fluids in later mobilisation of metals.

1. Introduction

Sulfur, though a minor constituent in silicate melts, exerts a major influence on magmatic redox state, volatile evolution, and metal fertility. Its speciation between sulfide and sulfate dictates the behaviour of chalcophile and siderophile elements, linking melt evolution to the formation of magmatic-hydrothermal ore deposits (Richards, 2015; Sillitoe, 2010). In emitted gases, the ratios of H_2S to SO_2 are used to detect renewed volcanic unrest (Aiuppa and Moussallam, 2024) and their concentrations also provide key constraints on magma storage and redox conditions (Hughes et al., 2024). The development of quantitative models which describe the behaviour of sulfur in magmas is thus fundamental for the understanding of magmatic and volcanic processes, as well as for assessing their environmental and planetary impacts (Gaillard et al., 2015; Oppenheimer et al., 2011).

The behaviour of sulfur and its partitioning between silicate melt, exsolved sulfide, and gas depends largely on its oxidation state. Sulfur dissolves in silicate melts predominantly as sulfide (S^{2-}) and sulfate (S^{6+} or SO_4^{2-}), substituting for O^{2-} in the melt (Boulliung and Wood, 2023, 2022; Fincham and Richardson, 1954; Métrich et al., 2009; O'Neill and Mavrogenes, 2022, 2002). Fincham and Richardson (1954) demonstrated that, in addition to temperature and melt composition, sulfur solubility is strongly dependent on the fugacities of oxygen (fO_2) and sulfur (fS_2). They showed that under reducing conditions (below the fO_2 of the fayalite-magnetite-quartz (FMQ) buffer approximately), sulfide solubility can be described by the equilibrium:

$$\frac{1}{2}S_{2\,(v)} + O^{2-}_{(m)} = \frac{1}{2}O_{2\,(v)} + S^{2-}_{(m)} \quad (1)$$

where subscripts *v* and *m* refer respectively to gas and melt phases. The equilibrium constant K_1 may be written as follows:

$$\log K_1 = \log\left(\frac{a^m_{S^{2-}} \cdot fO_2^{\frac{1}{2}}}{a^m_{O^{2-}} \cdot fS_2^{\frac{1}{2}}}\right) = \log\left(\frac{\gamma^m_{S^{2-}} X^m_{S^{2-}} \cdot fO_2^{\frac{1}{2}}}{\gamma^m_{O^{2-}} X^m_{O^{2-}} \cdot fS_2^{\frac{1}{2}}}\right) \quad (2)$$

In equation (2) a_i^m is the activity of species i in the melt, and X_i^m and γ_i^m are its mole fraction and activity coefficient, respectively. The fugacities of sulfur and oxygen are referenced to standard states of pure gas at 1 bar and the temperature of interest. As sulfur is typically low in concentration, the change in O^{2-} activity attending sulfur dissolution should be small such that $a^m_{O^{2-}}$ may be considered constant for a given melt composition. By combining the equilibrium constant ($\log K_1$) with $a^m_{O^{2-}}$, we define the sulfide capacity ($C_{S^{2-}}$) of the melt as follows:

$$\log C_{S^{2-}} = \log[S^{2-}] + \frac{1}{2}\log\frac{fS_2}{fO_2} = \log K_1 + \log a^m_{O^{2-}} \quad (3)$$

Here, [S^{2-}] is the sulfide concentration in the melt (normally in weight%). Sulfide capacity ($C_{S^{2-}}$) enables expression of the dependence of sulfide solubility on both temperature (through $\log K_1$) and melt composition (through $a^m_{O^{2-}}$). Under oxidising conditions (more than 1 $\log fO_2$ unit above FMQ; FMQ+1), sulfate (SO_4^{2-}), is the dominant sulfur species, and its solubility may be expressed by the heterogenous equilibrium:

$$\frac{1}{2}S_{2\,(v)} + \frac{3}{2}O^{2-}_{(m)} + O_{2\,(v)} = SO^{2-}_{4\,(m)} \quad (4)$$

And its associated equilibrium constant:

$$\log K_4 = log\left(\frac{a^m_{SO_4^{2-}}}{a^m_{O^{2-}} \cdot fS_2^{\frac{1}{2}} \cdot fO_2^{\frac{3}{2}}}\right) = \log\left(\frac{\gamma^m_{SO_4^{2-}} X^m_{SO_4^{2-}}}{\gamma^m_{O^{2-}} X^m_{O^{2-}} \cdot fS_2^{\frac{1}{2}} \cdot fO_2^{\frac{3}{2}}}\right) \quad (5)$$

Applying the same approximations as for the sulfide capacity (i.e. $\gamma^m_{SO_4^{2-}} = 1$; $a^m_{SO_4^{2-}} = [SO_4^{2-}]$; $a^m_{O^{2-}}$ = constant), the sulfate capacity ($C_{S^{6+}}$) may be defined as, with $[SO_4^{2-}]$ being the weight % sulfur in the melt:

$$\log C_{S^{6+}} = \log[SO_4^{2-}] - \frac{1}{2}\log fS_2 - \frac{3}{2}\log fO_2 = \log K_4 + \log a^m_{O^{2-}} \quad (6)$$

Equation (6) provides a thermodynamic framework for describing sulfur dissolution into silicate melt under oxidising conditions analogous to the sulfide capacity equation (3) which is applicable under reducing conditions.

Although fO_2 is clearly, from the above discussion, a major control on sulfur speciation in silicate melts, the role of temperature - particularly under geologically relevant conditions - remains debated. Early hydrous experiments on silicic melts revealed conflicting results. Luhr (1990) found little change in melt sulfur content between 800 and 1000°C at logfO_2 buffered near 0.7 logfO_2 units below the NNO buffer (NNO-0.7), while Carroll and Rutherford (1987) observed a strong positive temperature dependence under more oxidising conditions. The apparent inconsistency probably reflects a number of factors including differences in melt composition, temperature and water content all of which require resolution.

Recent experiments under anhydrous conditions have helped elucidate some of the potential factors which complicate the interpretation of sulfur solubility. Nash et. al., (2019), for example investigated the effect of bulk composition on the S^{6+}/S^{2-} ratio at fixed fO_2 and temperature in melts ranging in composition from Fe-rich martian basalt, through terrestrial basalt and andesite to dacite. They found, as expected, an abrupt increase in S^{6+}/S^{2-} with increasing oxygen fugacity above FMQ for all melts at 1300°C and that the region where both oxidation states are present corresponds closely to the fO_2 range measured in mid-ocean ridge basalts (MORB). They also showed that increasing FeO content in the melt stabilises S^{2-} to higher oxygen fugacity such that the martian basalt with 18% FeO has the same S^{6+}/S^{2-} as the dacite with 5% FeO at an oxygen fugacity 0.5 logfO_2 units higher. Although their experiments were isothermal, at 1300ºC, Nash et al., (2019) made a prediction, based on thermodynamic data for solid analogues, that the interval over which S^{2-} transforms with oxidation to S^{6+} shifts to higher logfO_2 values (relative to FMQ) with decreasing temperature. This implies that sulfide becomes relatively more stable at the lower temperatures typical of crustal magmas. The temperature trend was corroborated experimentally at 1200-1500°C by O'Neill and Mavrogenes (2002, 2022) and Boulliung and Wood (2022, 2023) who found, however, that the overall temperature effect appears small relative to the influence of melt composition and logfO_2. Natural observations, in contrast. suggest a much greater temperature effect on S^{2-} stability than that given by these high temperature ($\geq$1200°) data. Sulfide inclusions are widespread in arc phenocrysts and cumulates, even when melts appear too oxidised for sulfide stability (e.g. Humphreys et al., 2006; Chen et al., 2020). This

discrepancy suggests either that magmas undergo significant redox evolution as they crystallise or degas (Jenner et al., 2010; Lee et al. 2010; Burgisser and Scaillet, 2007), and/or that sulfide stability under crustal conditions is underestimated by high-temperature models.

In order to address the possibility that S^{2-} stability is enhanced at the lower temperatures typical of subduction zone magmatism, we have obtained new experimental data for sulfide and sulfate solubilities in silicate melts between 1050 and 1250°C. We investigated 14 silicate compositions using a 1 atm gas-mixing furnace with independently controlled fS_2 and fO_2. Sulfide and sulfate capacities were measured for each composition and were fitted to develop new models describing their solubilities as functions of temperature and melt composition. By combining our results with existing datasets, we provide improved constraints on the sulfide-sulfate transition under crustal conditions.

2. Experimental and Analytical Techniques

2.1 Starting material

Starting compositions used for the experiments in this study are reported in Table 1 and were selected to include a wide range of terrestrial rock compositions (e.g. SiO_2=38-64wt.%, FeO_{tot}=0-11.5wt.%, CaO=1.5-13.9wt.%, MgO=0.1-14.1wt.%). Synthetic starting compositions were prepared from mixtures of high purity oxide and carbonate powders that were combined and ground in an agate mortar under ethanol for ~ 1 hour, decarbonated overnight in air at 800 °C, and finally reground into fine powders. Starting compositions of the materials synthesized for this study were obtained after melting the powders onto Pt wire in air for ~5 minutes at 1300°C and 1 atm.

2.2 Experimental

Between 5 and 10 mg of starting material were combined with polyvinyl alcohol solution and placed on loops constructed from 0.25mm Pt wire. To minimise Fe-loss to Pt wire under reducing conditions (Grove, 1982), we pre-doped the wires with Fe. This was done by placing Icelandic basalt powder (FeOtot=9.0wt.%) on the wire which was then held under the same temperature and gas mixture

158 conditions as the experiments reported in Tables 2 and 3. Pre-conditioned Pt wire was soaked in room-
159 temperature hydrofluoric acid for several hours, rinsed with deionised water, and then loaded with
160 sample material. A typical experiment involved 7-8 samples that were attached to a "chandelier"
161 constructed from Pt-wire and suspended from a hooked silica rod.

162 Gas mixing experiments were carried out in a GERO vertical tube furnace (HRTV 70-250/18)
163 at atmospheric pressure. Oxygen and sulfur fugacities were imposed using mixtures of air and SO_2 to
164 access higher fO_2's and CO_2-CO-SO_2 for lower fO_2's. Oxygen and sulfur fugacities (shown in Tables 2
165 and 3) were calculated from thermodynamic data for the relevant C, O, and S bearing species taken
166 from the JANAF thermochemical tables (Chase, 1998; https://kinetics.nist.gov/janaf/) using the
167 computational procedure of White et al., (1958). Flow rates for each gas were controlled on individual
168 mass flow controllers (Omega FMA5500); total flow rates were maintained at ~200mL min^{-1}
169 corresponding to a linear flow velocity of ~0.23cm s^{-1}. The gas mixture for each experiment was allowed
170 to flow through the furnace at the desired experimental temperature for at least 20 minutes before the
171 experimental charges were lowered into the hot zone of the furnace.

172 Experiments were performed at temperatures between 1250 and 1050°C. Temperatures were
173 periodically monitored using an R and/or B -type Pt-Rh thermocouple positioned inside a sealed
174 alumina sleeve in the hot zone of the furnace. Measurements were found to remain within ±2°C of the
175 target temperature. Depending on temperature and starting composition, experiments were held at
176 temperature in the gas mixture for 24 to 120 hours. Experiment durations were determined from the
177 results of time-series tests equilibration tests (Fig. 1, see section 3.1). After equilibration, charges were
178 quenched by rapidly raising the chandelier to the cool region of the furnace. Run products were then
179 removed from Pt-loops, mounted in epoxy, polished, and carbon coated for electron microprobe
180 analysis.

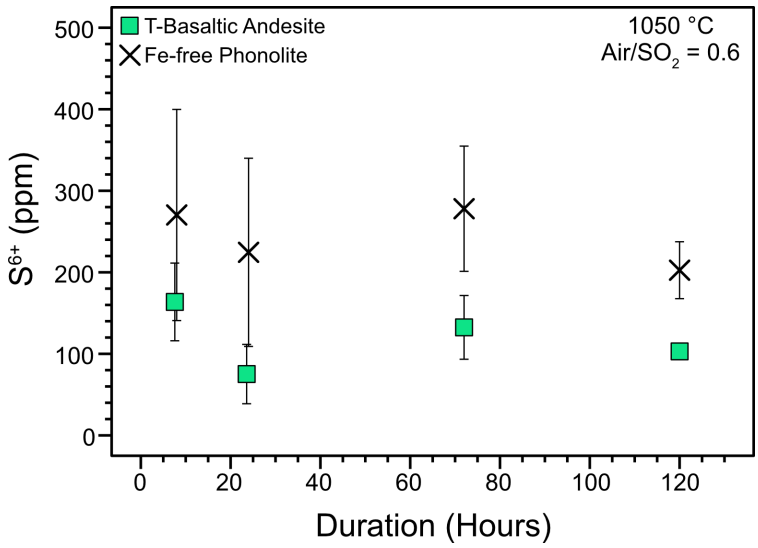

Figure 1. Sulfur contents (as S^{6+}) as a function of time measured in glasses using the T-basaltic andesite and Fe-free phonolite starting compositions run at 1050°C, 1 atm, log$f$O$_2$ = -1.2 (ΔFMQ +9.1), and log$f$S$_2$ = -18.7.

2.3 Analytical techniques

Major element and sulfur concentrations of all experimental glasses were determined using a CAMECA SX5-FEG electron microprobe analyser equipped with five wavelength dispersive spectrometers at the Department of Earth Sciences, University of Oxford. Analyses were carried out using an accelerating voltage of 15kV, a beam current of 20nA, and a spot size of 20µm. Counting times were 30 seconds on peak and 15 seconds for backgrounds except for K and Na which were reduced to 20 seconds peak and 10 seconds background in order to minimise element migration during analysis. These elements were analysed first on the relevant spectrometers. Primary standards used for calibrating peak position and intensities were albite for Na, Si, and Al, MgO for Mg, TiO$_2$ for Ti, sanidine for K, wollastonite for Ca, manganese for Mn, fayalite for Fe, and either galena or barite for when S was assumed to be all sulfide or sulfate in the glass, respectively. Detection limits for S were ~110ppm. A second analytical routine was used for glasses with S contents close to or below the detection limits. These glasses were reanalysed using a 60nA beam current, a 30µm spot size, and counting times were extended to 120 seconds on peak and 60 seconds on the background. This analytical routine yielded detection limits of ~20ppm for S. Glasses were reanalysed adjacent to the points where other elements had been previously measured and between 10-30 replicate analyses were collected per glass.

The Juan de Fuca basaltic glass VG-2 was used as a secondary standard for glasses containing reduced S. An average value of 1472±71ppm (n=18, 1s.d.) was obtained over three separate analytical sessions. This is in excellent agreement with the accepted values (S=1440±82ppm, 1s.d., n=34; compiled GeoReM values; Jochum et al., 2007).

3. Results

3.1 Attainment of equilibrium

Figure 1 shows the sulfur contents of silicate liquids from a series of experiments performed at 1050°C, with the SO_2/air gas mixture fixed at 0.6, across a range of experimental durations. Time-series experiments were conducted to assess the extents of equilibration between gas mixtures and silicate melt, with equilibrium assumed to correspond to the attainment of steady-state sulfur content in the glass. Melts approached constant sulfur concentrations (within analytical uncertainty) after 24 hours at 1050°C. However, extending run durations to 120 hours significantly reduced variability in glass sulfur contents, for example, from 29% to 6% relative standard deviations in the T-basaltic andesite composition. Based on these findings, subsequent experiments were run for 120 hours at 1050°C, 24 to 72 hours at 1100°C, and 24 hours at or above 1150°C.

3.2 Compositions of experimental products

Experimental product compositions and experimental conditions are summarised in Tables 2 and 3. Most of the compositions studied have dry liquidus temperatures above 1200°C, which resulted in many products containing both quenched glass and crystalline phases. Exceptions include experimental runs involving the T-basaltic andesite, T-andesite, and foidite under oxidising conditions, which remained entirely liquid down to 1050°C. Experimental products that contained little or no quenched glass were excluded from further analysis. Electron dispersive spectroscopy identified the crystalline phases as predominantly plagioclase, olivine, and clinopyroxene. In oxidising experiments ($\log fO_2$>-1.3), Fe-Ti oxides were also present, while crystalline -sulfides were observed in some charges held under reducing conditions ($\log fO_2$<-11).

Major element concentrations in quenched glasses (i.e. SiO_2, Al_2O_3, CaO, FeOtot, MgO, Na_2O, K_2O, TiO_2) commonly deviate from starting compositions due to crystallisation of silicate ± oxide ± sulfide phases. In contrast, glass-only products (T-basaltic andesite, T-andesite, and foidite) exhibit relatively minor variations (e.g. T-basaltic andesite: SiO_2=55.9±0.6wt.%, Al_2O_3=22.6±0.4wt.%), aside from small but variable losses of Na_2O and/or K_2O to the furnace atmosphere (e.g. Sugawara, 1999) and occasional Fe loss to Pt wires or to FeS precipitation under reducing conditions.

3.3 Sulfide and sulfate capacities as a function of temperature and melt composition

The effects of temperature and composition on sulfur capacities in experimental glasses are shown in Fig. 2 and the data on which these are based are given in Tables 2 and 3. Capacities were determined following the thermodynamic relationships defined by Fincham and Richardson (1954) (equations 3 and 6), using measured sulfur contents (wt.%) in combination with the experimental temperatures, fO_2, and fS_2 values. Uncertainties on $\log C_{S6+}$ and $\log C_{S2-}$ were estimated by combining the standard deviations on the measured sulfur contents and by allocating ±0.1 log unit uncertainties to $\log fO_2$ and $\log fS_2$.

Figure 2 is a plot of $\log C_{S2-}$ (panel A) and $\log C_{S6+}$ (panel B) against 1000/T for experiments in this study (green symbols) which are compared in the figure to the experimental glasses of Boulliung and Wood (2022, 2023) and O'Neill and Mavrogenes (2002, 2022). Results show that sulfide capacity decreases with decreasing temperature, which is consistent with previous studies. In Fe-free phonolite experiments, the absence of FeO, a key control on sulfide solubility, provides a clear view of the temperature dependence with $\log C_{S2-}$ increasing from -7.2 at 1050°C to -5.9 at 1200°C. In addition to temperature, melt composition has a strong effect on sulfide capacity. At 1050°C, $\log C_{S2-}$ increases from -7.2 in Fe-free phonolite to -6.2 in basanite and -6.1 in Fe-bearing phonolite. These differences correlate with increasing FeO content (in basanite) and K_2O content (in phonolite), confirming that melt composition exerts a significant control on sulfide solubility.

Sulfate capacities increase with decreasing temperature and, like sulfide capacities, are compositionally dependent. In Fe-free phonolite, for example, sulfate capacity ($\log C_{S6+}$) increases from 8.2 at 1250°C to 9.7 at 1050°C. At 1050°C, $\log C_{S6+}$ values range from 9.4 in the T-andesite to 10.6 in phonolite, with intermediate values such as 10.3 in the T-basaltic andesite. These differences correlate with increasing Na_2O and CaO contents in the melt, confirming previous findings that CaO and Na_2O content promote sulfate stability.

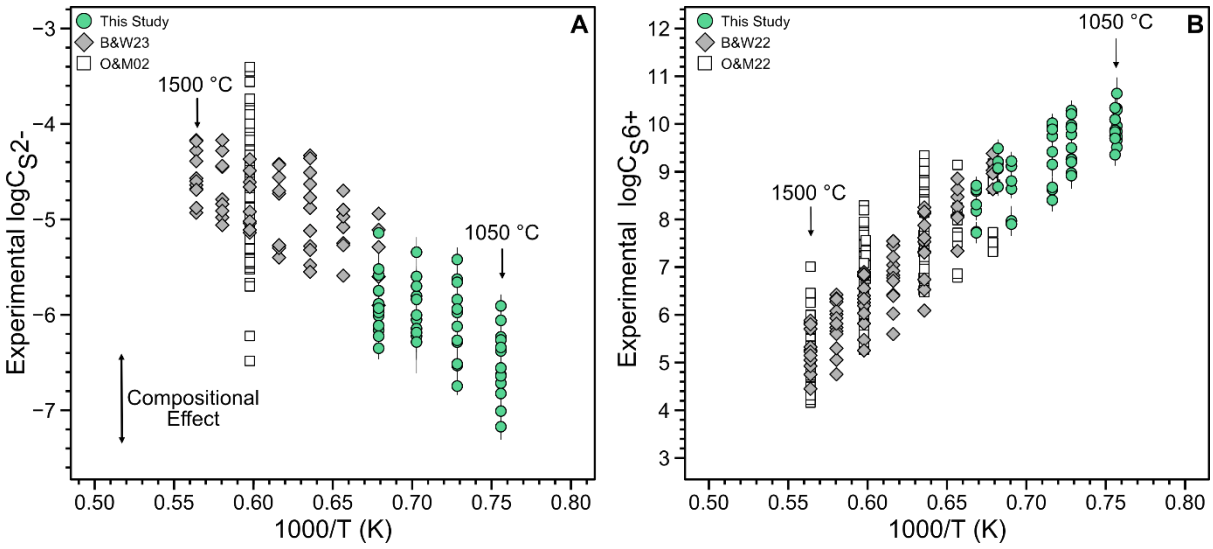

Figure 2. Experimental sulfide (A) and sulfate (B) capacities plotted as a function of reciprocal temperature ($1/T * 10^3$). Experimental glasses from this study are shown as green points. For comparison, sulfide and sulfate capacities obtained in 1 atm experiments are given as grey diamonds from the study of Boulliung and Wood 2022, 2023 (B&W23 and B&W23) and white squares from work of O'Neill and Mavrogenes 2002, 2022 (O&M02 and O&M22). Error bars represent errors on measured sulfur contents combined with ± 0.1 on $\log fS_2$ and $\log fO_2$.

3.4 Describing sulfide and sulfate capacities as functions of temperature and composition

In order to develop comprehensive models of sulfide and sulfate capacities, we restricted our dataset to experimental silicate glasses produced at 1 atm, where fS_2 and fO_2 were explicitly and accurately known, and where sulfur speciation in the melt was constrained to be exclusively as either sulfide or sulfate. We excluded experimental data where mixed valence states were expected or observed (e.g., Nash et al., 2019). This ensures that sulfide and sulfate capacities can be reliably

constrained using established thermodynamic relationships. The selected literature dataset spans temperatures from 1200 to 1500°C and encompasses a broad range of silicate melt compositions (e.g. SiO_2=36.69-75wt.% FeO=0-19wt.%, CaO=0-45.9 wt.%, Na_2O=0-11.6wt.%.

To maintain consistency with our own experiments, we recalculated fS_2 and fO_2 values for each literature dataset using the reported gas mixtures and experimental temperatures. Sulfide and sulfate capacities were then calculated from the reported sulfur contents using Equations 3 and 6. Experimentally determined capacities were fit to a model that relates composition and temperature using a functional form adopted from reciprocal solution theory (Wood and Nicholls, 1978):

$$\log C_{S^z} = A_0^{Sz} + \frac{B_o^S}{T} + \sum_{M} \frac{X_M A_M}{T} \quad (7)$$

Where A_0^{Sz} and B_o^S are constants for a given S species (z), X_M are the oxide mole fractions on a single-oxygen basis, and A_M are coefficients that derive from the differences between the standard state free energies μ° of formation of the oxide and sulfide or sulfate components of interest (assuming ideal mixing; e.g. $\Delta G^\circ = \mu^\circ_{M_{2/z}O} - \mu^\circ_{M_{2/z}S}$; $\Delta G^0 = \mu^\circ_{M_{\frac{2}{z}}O} - \mu^\circ_{M_{2/z}SO_4}$). All glass compositions used were recalculated to mole fractions on a single-oxygen basis of $Si_{0.5}O$, $Ti_{0.5}O$, $Al_{0.67}O$, MnO, $FeO^{(2+)}$, $Fe_{0.67}O^{(3+)}$, MgO, CaO, Na_2O, and K_2O to the sum of 1. Proportions of Fe^{3+} and Fe^{2+} were calculated using the parameterisation of Kress and Carmichael (1991; their eq. 7).

To relate sulfide and sulfate capacities to temperature and melt composition, we implemented LASSO regression using the glmnet package (Friedman et al., 2010) in R (version 4.3.1). The optimal penalty parameter (λ) was tuned by repeated (n = 100) Monte-Carlo 20-fold cross-validation. For each iteration we kept the value of λ that was within 1 standard error of the minimum mean squared error (MSE) and the average of those 100 λ values was taken as our final penalty. The full dataset was then refit using LASSO with this final λ value to obtain the model coefficients and uncertainties. Separate LASSO regressions were performed for sulfide and sulfate capacity datasets. All model inputs were standardised, and predictor variables included single-oxygen mole fractions of major oxides divided by

294 temperature, following the functional form in equation (7). Calibration data and R script used for model
295 fitting are provided in the supplementary materials.

296 **3.4.1 Sulfide capacity**

297 Fitting the experimentally derived sulfide capacities, 48 data points from this study and 257
298 from the literature, to equation (7) resulted in the following expression:

299 $$\log C_{S^{2-}} = 0.30 + (-2935X_{Si_{0.5}O} + 19298X_{FeO} - 1303X_{Na_2O} + 11423X_{K_2O} - 7261) / T$$
300 (8)

301 Where T is in kelvins. This model yields a root mean square error (RMSE) of 0.21 and R^2 is 0.91.
302 Notably, the temperature and FeO terms are nearly identical to those in the parameterisation of
303 Boulliung and Wood (2023), suggesting that the temperature dependence derived by Boulliung and
304 Wood from 1200-1500°C data also closely fits our 1050°C data.

305 We examined the differences between predicted and measured $\log C_{S2-}$ values for systematic
306 trends with temperature and melt composition. No clear relationship emerged, although the largest
307 residuals were generally associated with melts characterised by high Al_2O_3, Na_2O, K_2O, and low FeO
308 contents. To account for these effects, we tested additional compositional cross-terms which take the
309 form $X_iX_jA_{ij}$ (e.g. $X_{Si0.5O}X_{Al0.7O}$ or $X_{FeO}X_{Na2O}$). We also tested the inclusion of an FeO-dependent
310 sigmoidal term (erf(X_{FeO})) which was found to be significant in the sulfide capacity model of O'Neill
311 (2021). Incorporating these additional terms, we obtained the following improved parametrisation:

312 $$\log C_{S^{2-}} = 0.65 + \big(-3368X_{Si_{0.5}O} - 1233X_{Al_{0.6}O} + 1295X_{CaO} + 44885X_{K_2O} + 10914X_{FeO} \cdot X_{Si_{0.5}O}$$
313 $$- 871864X_{FeO} \cdot X_{K_2O} - 225569X_{FeO} \cdot X_{Na_2O} + 54392X_{FeO} \cdot X_{Al_{0.5}O} - 7585\big) / T$$
314 $$+ 3.9\,\mathrm{erf}[X_{FeO}] \quad (9)$$

315 This second model achieves a lower RMSE of 0.16 and R^2=0.93, indicating a significant
316 improvement in predictive performance. Importantly, the 1/T coefficient remains nearly unchanged,
317 reaffirming that much of the residual misfit in the simpler model was due to unaccounted compositional

effects rather than temperature dependence. As in Smythe et al. (2017) and O'Neill (2021), we find the $FeO{\cdot}Si_{0.5}O$ interaction to be highly significant and K_2O also emerged as an important control.

3.4.2 Sulfate Capacity

We fit equation (7) to 51 experimentally derived $\log C_{S^{6+}}$ values from this study and 351 values from the literature, resulting in the following parameterisation:

$$log C_{S^{6+}} = -11.11 + (8989X_{MnO} + 5633X_{MgO} + 17422X_{CaO} + 31725X_{Na_2O} + 26845) / T \quad (10)$$

This regression yields an RMSE of 0.31 and R^2=0.94. The intercept (A_0) term is only slightly larger than that of Boulliung and Wood (2023) (A_0=-12.9). The estimated temperature dependence is similar in both studies. Inspection of the residuals, however, revealed systematic curvature at temperatures below 1150°C, indicating a deviation from the assumed linear relationship between $\log C_{S^{6+}}$ and 1/T. Similar non-linearity was noted by Boulliung and Wood (2023) near 1200°C. To account for this, we introduced a logT term, yielding the following improved fit:

$$\begin{aligned} log C_{S^{6+}} = {} & 196.0 \\ & + \left(-7633X_{Si_{0.5}O} - 10670_{Ti_{0.5}O} - 6901X_{Al_{0.6}O} - 4625X_{FeO_T} + 19114X_{MnO}\right. \\ & \left. + 11740X_{CaO} + 33267X_{Na_2O} - 4095\right) / \ T \ - 57.3\log(T) \quad (11) \end{aligned}$$

This updated fit significantly improves the model performance, reducing RMSE to 0.26 and increasing R^2 to 0.97. Among compositional predictors, CaO and Na_2O were found to exert the strongest positive control on sulfate capacities which is consistent with previous studies (Boulliung and Wood, 2022;2023; O'Neill and Mavrogenes 2022).

4. Discussion

4.1 Comparison to other sulfide and sulfate capacity models

Figure 3 compares predicted sulfide and sulfate capacities calculated using equations (9) and (11), from this work, with published experimental data collected at 1 atm over a temperature range of

1050-1500°C. Also shown are model predictions from Boulliung and Wood (2023; their eqs. 7 and 11), O'Neill and Mavrogenes (2022), and O'Neill (2021). All models reproduce experimental $\log C_{S^{2-}}$ and $\log C_{S^{6+}}$ values well at and above 1200°C, the overlapping temperature range across which the models were calibrated. In the temperature range below 1200°C, however, some scatter is observed in the experimental measurements of $\log C_{S^{2-}}$ when compared to the predictions of the Boulliung and Wood (2023) and O'Neill (2021) models. The scatter is probably mainly due to the analytical uncertainties in the low sulfur concentrations observed at low temperature. Median sulfur contents at, for example, 1050°C are ~350ppm, compared to ~800ppm at 1200°C.

Observed sulfate capacities, expressed as $\log C_{S^{6+}}$ are generally well reproduced by all models at temperatures above 1200°C. At lower temperatures (below 1200°C), $\log C_{S^{6+}}$ model performance diverges significantly. Both the Boulliung and Wood and the O'Neill and Mavrogenes models increasingly overpredict $\log C_{S^{6+}}$ values as temperature decreases. This overestimation becomes pronounced at 1150 and 1100°C, with many data points falling outside the 1:1 line. Below 1100°C, however, both the Boulliung and Wood (2023) and O'Neill (2021) models consistently overestimate sulfate solubility by 1-2 orders of magnitude. The misfit is systematic and significant: all 1050°C data fall well outside their respective 95% confidence intervals. In contrast, the prediction intervals from our model remain within the 95% CI across all lower-temperature data. This improved performance stems from the inclusion of a logT term, which captures the strong non-linear decrease in sulfate solubility observed below 1200°C.

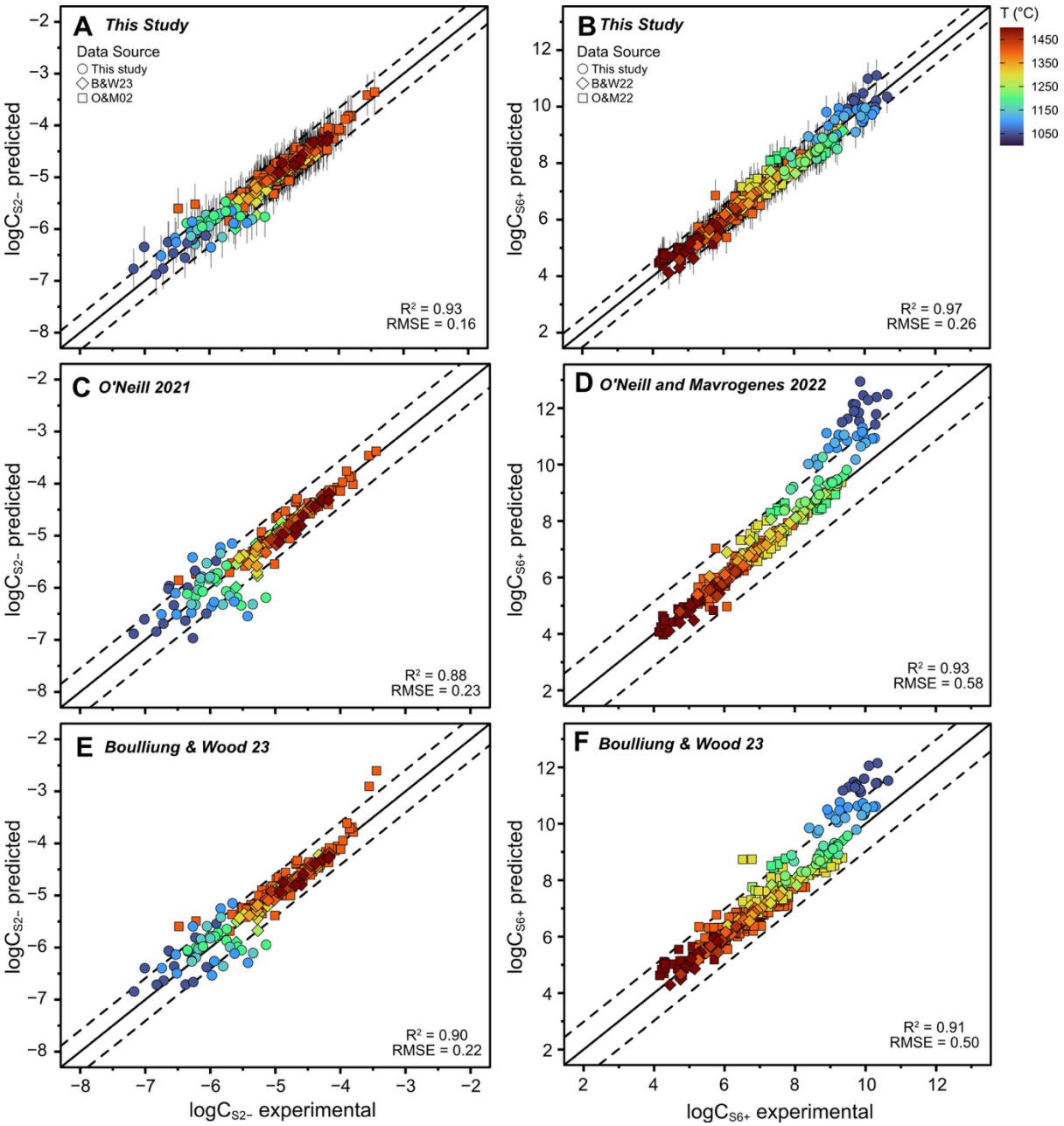

Figure 3. Experimental versus predicted sulfide (left) and sulfate (right) capacities calculated using equations 9 (**A**) and 11 (**B**) for all 1 atm experimental data used in model calibration. Compared are the model predictions of O'Neill (**C**; 2021) and O'Neill and Mavrogenes (**D**; 2022); Boulliung and Wood (2023; panels **E** and **F**; their eqs. 7 and 11). Symbols denote data sources: circles are this study; diamonds are Boulliung and Wood (2022, 2023; B&W22 and B&W22); squares are O'Neill and Mavrogenes (2002, 2022; O&M02 and O&M22). Symbols are coloured as a function of experimental temperatures (°C). The solid lines in each panel are 1:1 lines, dashed lines show the ± 95% confidence intervals of the fit ($CI_{logCS2-}$ ± 0.31 and $CI_{logCS6+}$ ± 0.51), while error bars in **A** and **B** are point-based 95% prediction intervals (PI) giving average values of $PI_{logCS2-}$ ± 0.39 and $PI_{logCS6+}$ ± 0.57. Plotted data are given in supplementary materials (Supp. 1).

4.2 Temperature dependence of the sulfide to sulfate crossover

The main goal of this study was to determine the temperature effects on sulfide and sulfate solubilities and speciation. We therefore begin by evaluating the temperature effect on the fO_2 of the crossover from S^{2-} to S^{6+} stability by applying our experimental solubility models to a suite of natural melt compositions at temperatures between 1050 and 1500°C. The oxidation state of sulfur in silicate melts as a function of logfO_2 - expressed as S^{6+}/S^{2-} - can be solved analytically by combining equations 3 and 6:

$$\log\left(\frac{[SO_4^{2-}]}{[S^{2-}]}\right) = \log\left(\frac{C_{S^{6+}}}{C_{S^{2-}}}\right) + 2\log fO_2 \quad (12)$$

An excel-based calculator implementing these expressions is provided in the supplementary material. The results of such calculations are illustrated in Figs. 4 and 5.

Our model predicts that, as temperature decreases from 1200°C to 1050°C, the S^{2-}-S^{6+} crossover increases by approximately +0.6 log units in logfO_2 relative to the FMQ buffer, nearly independent of melt composition. The pronounced temperature dependence (relative to FMQ) arises from the large negative logT coefficient in our sulfate solubility model, which increasingly favours sulfide stability as temperature decreases. When extrapolated below their ranges of calibration, previous models significantly underestimate this effect. The O'Neill and Mavrogenes (2022) model, calibrated between 1500 and 1200°C, predicts a shift of only +0.22 logfO_2 units from 1200 to 1050°C. Similarly, the

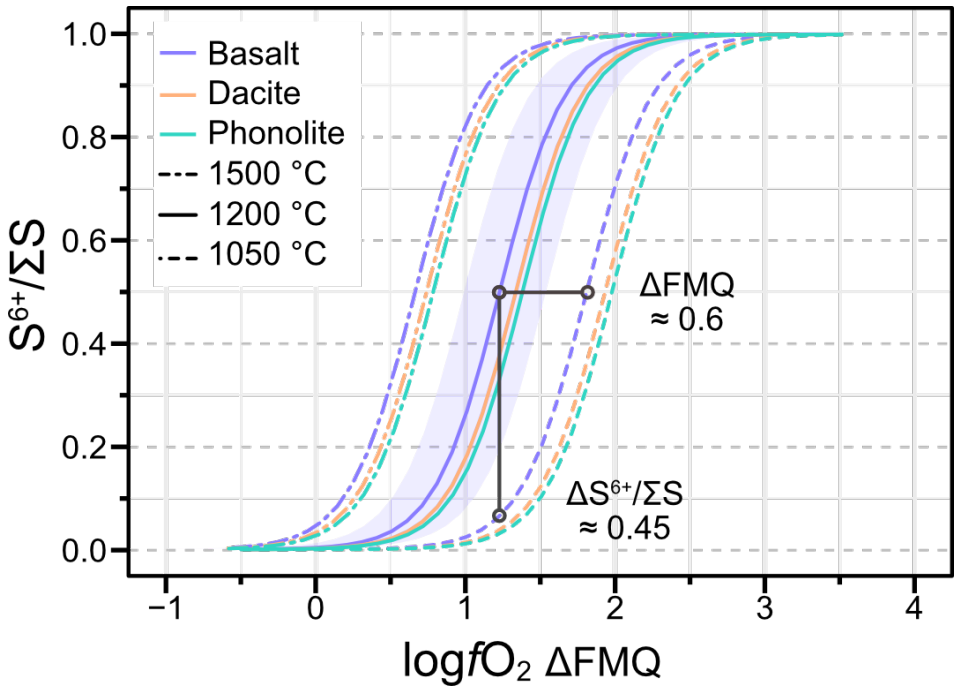

Figure 4. Sulfur speciation (fraction sulfate) versus logfO_2 relative to the FMQ buffer for Icelandic basalt (blue), dacite (orange), and phonolite (green). Dot-dash lines are 1500°C, solid lines are 1200 °C; dashed lines are 1050 °C. Cooling from 1200 to 1050 °C shifts the sulfide to sulfate transition to higher logfO_2 ΔFMQ by ~ 0.6 log units, meaning that - at a constant value of ΔFMQ and melt composition - sulfide is preferentially stabilised relative to sulfate. For example, at a fixed value of ~ ΔFMQ +1.25 a basaltic melt that has 50 % sulfate at 1200 °C would have ~5 % sulfate at 1050 °C. The blue shaded region denotes the 95 % confidence interval on the model predictions. For clarity uncertainties are shown only for the basalt model at 1200 °C but are representative of the errors associated with all plotted model curves. These are propagated from estimated CIs of ± 0.55 on logC_{S6+}, ± 0.35 on log$_{CS2-}$, and an assumed value of ± 0.1 s.d. on logfO_2. Curves for each composition were calculated using the major oxide compositions listed in Table 1.

Boulliung and Wood (2023) model yields a shift of +0.43 log units using a linear-T fit, and +0.14 with their logT expression. In contrast, our model - calibrated down to 1050°C - predicts a much larger shift of +0.6 log units. Notably, all models converge at and above 1200°C, suggesting that earlier formulations remain valid at high temperatures but fail to capture the stronger temperature sensitivity of sulfate solubility at lower magmatic conditions.

4.3 The combined effects of temperature, pressure, major element composition and water content

A long-standing goal in petrology is the development of a thermodynamically- grounded model that predicts sulfur speciation along the mantle-to-surface paths of magmas. Water-bearing experiments have dominated prior efforts to investigate sulfur speciation below 1200°C because of the powerful effects of H_2O on lowering the liquidus temperatures and viscosities of relevant melts. This approach introduces further complications, however, by making $\log fO_2$ dependent on H_2O content and $\log fS_2$ difficult to control or measure (Botcharnikov et al., 2010; Clemente et al., 2004; Jugo et al., 2010; Kleinsasser et al., 2024; Lesne et al., 2015; Matjuschkin et al., 2016). For these reasons we have deliberately sought melt compositions which are liquid below 1200°C at 1 atm enabling us to provide the first anhydrous dataset at <1200°C. This provides a baseline from which the effects of fO_2, fS_2 temperature and H_2O content can be evaluated independently.

We began by developing our sulfide and sulfate capacity expressions at 1 atm with the addition of a pressure term. We followed Boulliung and Wood (2023) who estimated the pressure term from solid molar volumes for $FeS + CaO + 2O_2(g) = FeO + CaSO_4$. The solids, ignoring O_2 which has a 1 bar standard state, give $\Delta V \approx 23$ cm³ mol^{-1} and lead to, for the S^{2-} to S^{6+} crossover:

$$\log fO_2(\text{P bar}) = \log fO_2(1\text{ bar}) + 0.06(\text{P}-1)/\text{T} \quad (13)$$

At crustal conditions the calculated effect is small so that raising pressure from 1 bar to 2 kbar should displace the sulfide-sulfate crossover by roughly 0.1log unit to lower $\log fO_2$ values relative to the FMQ buffer. This estimate has recently been experimentally corroborated by Muth and Cottrell (2025) who performed experiments on hydrous basaltic andesite at 1380°C and 1.5 and 3GPa. They used XANES spectroscopy to determine $S^{6+}/\Sigma S$ for the quenched glasses and found a pressure effect virtually identical to the estimate of Boulliung and Wood (2023).

Currently there are no direct experimental observations of the effects of water on sulfide and sulfate capacities. However, both O'Neill and Mavrogenes (2022) and Boulliung and Wood (2023) have

argued, based on hydrous experiments of Jugo et al. (2010) and Botcharnikov et al. (2011) that the effects of H_2O on the S^{6+}/S^{2-} ratio should be small. The reason is that the calculated fO_2 of the crossover at 0.2GPa and 1050°C is, assuming that H_2O is an ideal diluent, in good agreement with that calculated from the anhydrous models. We therefore treat H_2O, to first order, as an ideal diluent of the oxide components. In practice, adding 3-5wt.% H_2O is calculated to produce a small left-shift of the speciation curve (order 0.1-0.2 in ΔFMQ), favouring sulfate at fixed T.

Figure 5a compares our predicted $S^{6+}/\Sigma S$ at 1050 and 1100°C, 2kbar and 3wt.% H_2O with the thermodynamic models of Clemente et al. (2004; rhyolite, 2kbar, 4.5wt.% H_2O, 1100°C) and Lesne et al. (2015; basalt, 2kbar; 1050°C, 3wt.% H_2O). Agreement is excellent-their curves and ours are essentially coincident (within-error) across the transition region. Also shown is the XANES-based sulfur-speciation model of Jugo et al. (2010) calibrated on experimental basaltic glasses run at 1050°C**,** 2kbar**,** and containing ~2.5-4.5wt.% H_2O; it plots 0.6 log units lower in logfO_2 than our 1050°C prediction and similarly below the results of Lesne et al., (2015) on basalt. Part of the difference between our results and the Jugo et al., (2010) results can be explained by the leftward shift of 0.1-0.2 logfO_2 units produced by the presence of water in the Jugo et al., experiments. This still leaves a discrepancy between the results of Jugo et al., (2010) and those of Lesne et al., (2015), both on hydrous basalt, however. We suggest that some of this discrepancy may be due to problems of beam-induced redox changes as well as uncertainties in the fitting and interpretation of sulfur XANES data (Lerner et al., 2021; Métrich et al., 2009; Wilke et al., 2008).

Figure 5a shows that our calculated S^{2-}—S^{6+} crossover at 1050-1100ºC is in excellent agreement with most previous observations. Fig 5b indicates that our equations can also be extrapolated to lower temperatures. This figure shows that, at lower crustal pressures (1.0-1.5GPa), our 850-950°C**,** 5wt.%

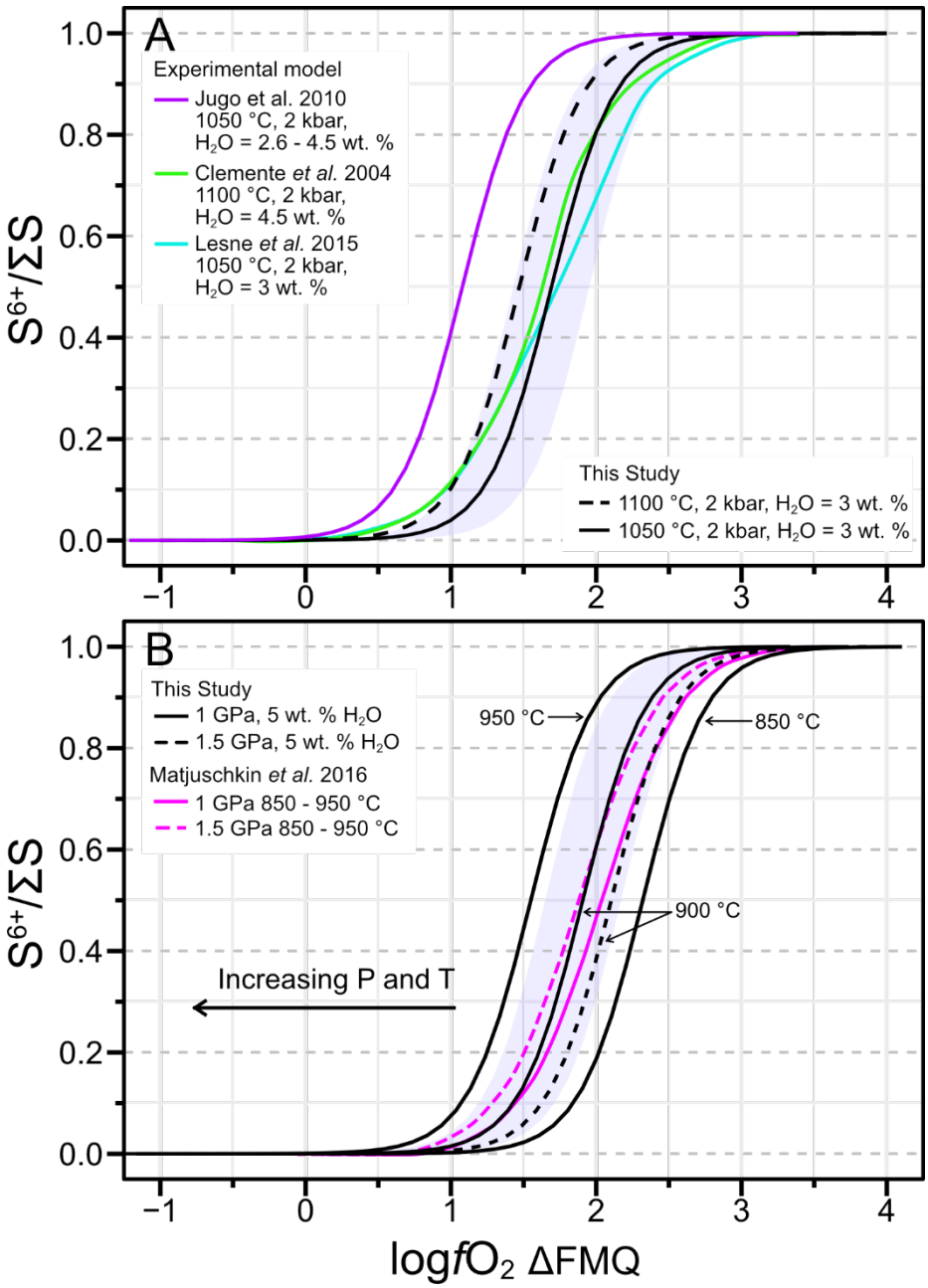

Figure 5. Comparison of $S^{6+}/\Sigma S$ predicted by this study with hydrous experimental models. Calculations from this study include a pressure term and treat H_2O as an ideal diluent (see section 4.3 of text). (**A**) Model curves for an Etna basalt (composition after Lesne et al., 2015) at 2 kbar, 3 wt.% H_2O, at 1050°C (solid black) and 1100°C (dashed black). Experimental models shown for comparison: Jugo et al. (2010), 1050°C, 2 kbar, Etna basalt with 2.6-4.5 wt.% H_2O (purple); Lesne et al. (2015), 1050°C, 2 kbar, Etna basalt with 3 wt.% H_2O (blue); Clemente et al. (2004), 1100°C, 2 kbar, rhyolite with 4.5 wt.% H_2O (green). (**B**) Model curves from this study at 850, 900, and 950°C, 1 GPa (solid black), and at 900°C, 1.5 GPa (dashed black). Experimental model of Matjuschkin et al. (2016) for trachyandesite with ~ 6.5 - 9.5 wt.% H_2O, 850-950°C: 1 GPa (pink dashed) and 1.5 GPa (pink solid). For clarity, model errors are shown only for our 1050 °C (**A**) and 900 °C, 1 GPa (**B**) model curves (following Fig. 4).

H_2O curves (Fig 5b) align closely with the Matjuschkin et al. (2016) speciation model. Matjuschkin et al. (2016) inferred a large shift of the sulfide-sulfate transition with pressure to higher relative fO_2. When we apply our equations at the exact experimental temperatures and pressures, however, we find that the pressure shifts inferred by Matjuschkin et al. (2016) are predominantly due to temperature differences, as suggested by Nash et al. (2019). The pressure effect is also positive in fO_2 but small and in agreement with equation (13).

In summary, comparisons of calculated S^{2-}-S^{6+} crossovers with experimental data show that temperature exerts the dominant control on sulfur speciation below 1200°C. Pressure produces only minor shifts in the sulfide-sulfate transition under crustal conditions. Melt composition plays a secondary role, and it appears that treating H_2O as an ideal diluent of oxide components captures the effects of water observed experimentally; the close agreement between model predictions and experimental datasets suggests that H_2O does not significantly modify sulfide or sulfate solubilities. Overall, temperature emerges as the primary driver of $S^{6+}/\Sigma S$ variations under crustal conditions, with pressure, composition, and H_2O exerting comparatively minor effects.

4.4 Influence of Fe-S redox exchange on the oxidation state of differentiating magmas

Arc magmas are systematically more oxidised than MORB, but the processes responsible remain debated. A widely held view is that arc melts inherit their high oxidation states from a mantle wedge modified by slab-derived fluids and sediments (Evans and Tomkins, 2011; Padrón-Navarta et al., 2023). An alternative hypothesis is that magmas oxidise internally during ascent and differentiation, rather than reflecting conditions in their source regions (Lee et al., 2010). Sulfur is central to addressing this question as arc magmas are both hydrous and sulfur-rich compared to MORB. Because both Fe and S are multivalent and abundant, their coupled speciation must strongly influence the redox trajectories of differentiating magmas.

To examine the interactions between fO_2 and the oxidation states of iron and sulfur, we modelled the co-evolution of $Fe^{3+}/\Sigma Fe$ and $S^{6+}/\Sigma S$ along polybaric fractional-crystallisation paths typical for calc-alkaline fractionation series (Marxer et al., 2023). Pressure, temperature, and major element

compositions for the modelled liquid lines of descent (LLD) were obtained using MAGEMin (Riel et al., 2022; Supp. 4) for a primitive hydrous arc basalt (Ulmer et al., 2018; 3wt.% H_2O). We tested three initial redox states (ΔFMQ= 0, +0.5, and +1.0) and two bulk sulfur contents (Stot=0.10 and 0.20wt.%). At each step along the LLD, fO_2 was solved numerically to balance the redox couples of Fe^{3+}/Fe^{2+} and S^{6+}/S^{2-} while conserving total FeO and S. Iron speciation was related to $\log fO_2$ using the model of Kress and Carmichael (1991). Sulfide saturation was tracked using the SCSS model of Fortin et al. (2015), calibrated for hydrous calc-alkaline systems. Once saturation is reached, S^{2-} and Fe^{2+} are extracted as a sulfide phase, and budgets are updated accordingly. It should be noted that the derived S^{2-} contents of the melts at sulfide saturation (SCSS) are upper bounds partly because we have excluded Cu and Ni, both of which lower SCSS (Ariskin et al., 2013; Smythe et al., 2017), and partly because we have extrapolated the model of Fortin et al. (2015) into the region where sulfide melt should crystallise a stable monosulfide solid solution (MSS). These approximations mean that the calculated extent of sulfide extraction is a conservative minimum.

Our results predict that Fe-S electron exchange can generate substantial self-oxidation during ascent, provided the initial melt contains a modest amount of S^{6+} (Fig. 6). For the pressure and temperature conditions tested here, this requires either bulk sulfur contents >0.1wt.% and/or initial redox states above ~FMQ+0.2. Under these conditions, fO_2 may increase by +2 to +3 log units relative to FMQ before fluid saturation occurs, beyond which degassing-driven redox changes are expected (Brounce et al., 2017; Burgisser and Scaillet, 2007). This progressive oxidation requires the presence of some S^{6+} at the onset of crystallisation. As the melt cools, S^{6+} is progressively reduced to S^{2-}, and the associated electron transfer oxidises Fe^{2+} to Fe^{3+}. The extent of oxidation is therefore governed jointly by the initial melt fO_2 and the total sulfur content.

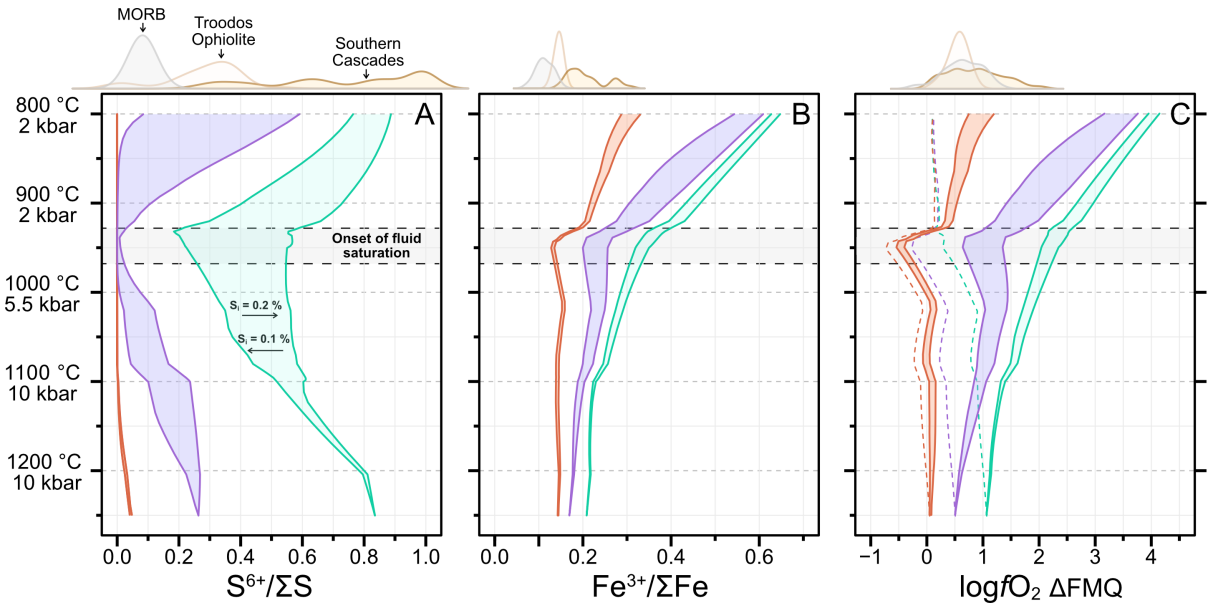

Figure 6. Fe-S redox exchange calculated along liquid lines of descent for calc-alkaline magmas. Calculations used P-T paths and melt major-element compositions obtained from MAGEMin which were used as inputs to our Fe-S redox model (Supp. 4). In panel (**C**), dashed lines indicate the evolution of logfO_2 from fractional crystallisation predicted by MAGEMin alone (no Fe-S redox exchange), used as a baseline for our calculations. Results are shown for three initial redox states: ΔFMQ (orange), ΔFMQ +0.5 (purple), ΔFMQ +1 (green) and two bulk sulfur contents of 0.1 wt.% (left edge of shaded fields) and 0.2 wt.% (right edge of shaded fields). The grey shaded region marks the onset of fluid saturation, assuming 0.1 wt.% CO_3^{2-} in the melt and using the H_2O and S contents from MAGEMin and Fe-S redox modelling results, respectively. Kernel density estimates above each panel compare measured $S^{6+}/\Sigma S$, $Fe^{3+}/\Sigma Fe$, and calculated logfO_2 values in MORB glasses (Berry, et al. 2018; Lerner 2021), Troodos Ophiolite (Saper, et al. 2024), and from the Cascades arc (Muth and Wallace, 2021). These calculations indicate that higher initial S^{6+} contents-arising from greater sulfur contents or slightly more oxidising starting conditions-drives stronger oxidation during ascent and crystallisation via Fe-S redox exchange.

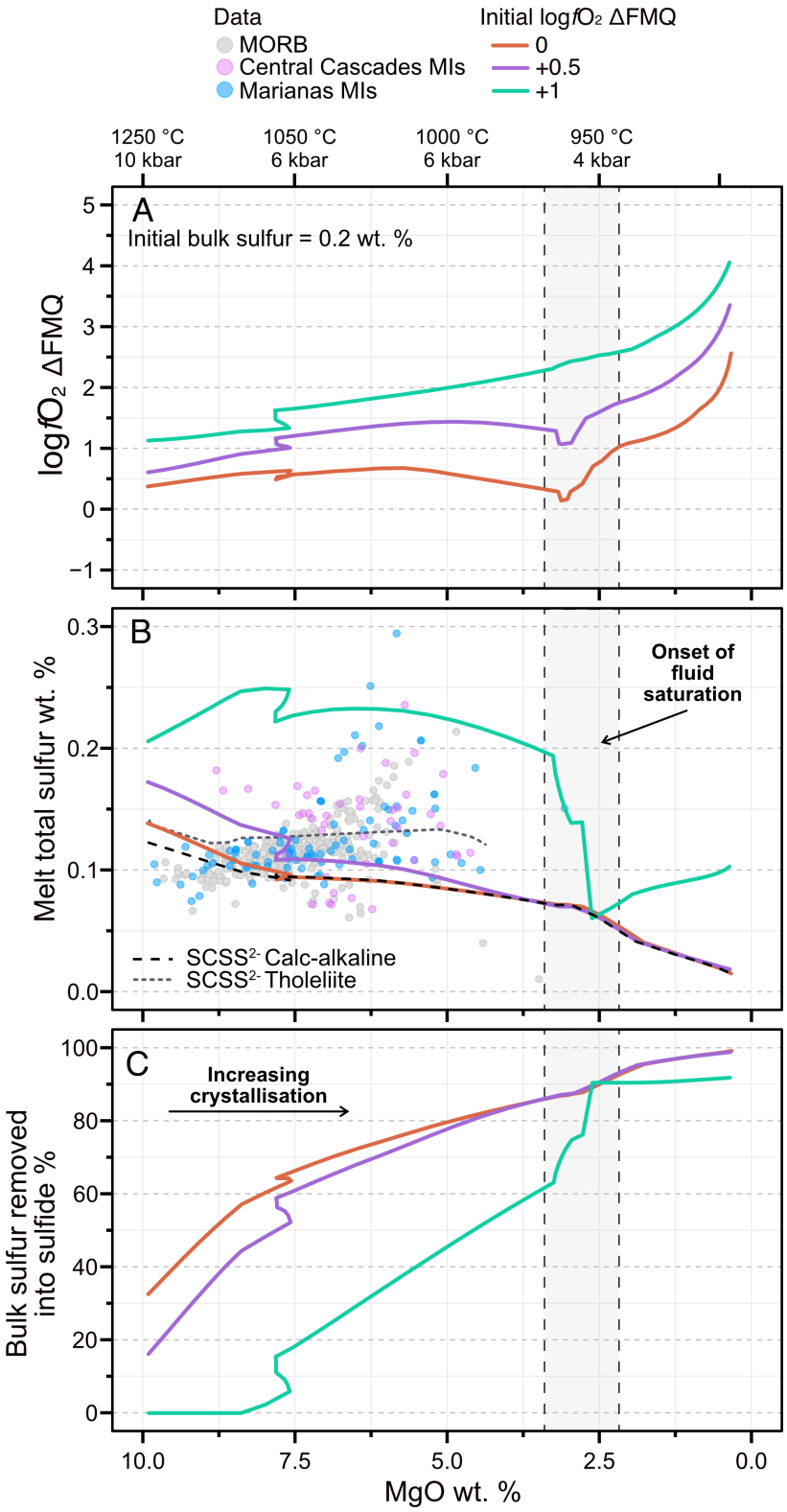

527 **Figure 7.** Comparison of MgO wt. % contents with evolving logfO_2 relative to the FMQ buffer (**A**);
528 total dissolved sulfur (**B**); and % of initial bulk sulfur captured in sulfide (FeS) (**C**) during Fe-S redox
529 exchange modelled along a calc-alkaline magma liquid line of descent (LLD). Results are shown for
530 three initial redox states: ΔFMQ (orange), ΔFMQ +0.5 (purple), ΔFMQ +1 (green), all having a bulk
531 sulfur content of 0.2 wt.%. Major elements, P, T, and baseline logfO_2 values used in our modelling were
532 obtained from MAGEMin (See section 4.4. of text for details). Corresponding $SCSS^{2-}$ values for our
533 modelled calc-alkaline magmas used in our calculations (black dashed; Fortin et al., 2015) are given in

panel (**B**), also included are $SCSS^{2-}$ values for a tholeiitic composition representative of MORB melts at ~FMQ (black dotted). Melt-inclusion sulfur and MgO compositions from the Cascades arc (pink circles) and the Mariana arc (blue circles) are overlain from Brounce et al., (2014); Kelley et al., (2010); Rowe et al., (2009); Ruscitto et al., (2010); and Shaw et al., (2008); MORB glass compositions (grey circles) are from Jenner and O'Neill (2012). Vertical grey shaded fields mark the range in saturation pressures and are calculated assuming 1000 ppm CO_3^{2-}, using the H_2O and sulfur contents from MAGEMin and Fe-S redox modelling results, respectively. Model results indicate that calc-alkaline magmas intersect and remain at (or above) sulfide saturation through much of their differentiation trajectory-even under oxidising conditions.

Progressive reduction of sulfur and oxidation of iron during cooling helps explain why arc magmas are systematically more oxidised than MORB. In MORB, high eruption temperatures (>1200°C) and low initial fO_2 favour S^{2-}, limiting S^{6+} availability and suppressing Fe-S redox exchange (Muth and Cottrell, 2025). Arc magmas, in contrast, are both cooler and more sulfur-rich (Wallace, 2005), making them predisposed to internal oxidation during crustal differentiation.

The strong temperature-dependence of sulfur speciation means that, even at high oxygen fugacities (>FMQ+2), our modelled melts retain sufficient S^{2-} to remain at sulfide saturation (Fig. 7c) during ascent. Cooling during ascent shifts equilibrium toward S^{2-}, promoting sulfide saturation despite elevated fO_2. This reconciles the paradox of oxidised arc magmas that continue to lose sulfur to sulfide phases and is consistent with the occurrence of sulfides in oxidised arc magmas (Humphreys et al., 2006; Georgatou et al., 2018), and cumulates (Chen et al., 2020; Cox et al., 2019).

In summary, Fe-S redox coupling offers a mechanism for dynamic oxidation of arc magmas during ascent, while simultaneously allowing sulfide saturation to persist. This dual effect provides a framework for understanding both the redox evolution of subduction-related magmas and the coexistence of highly oxidised melts with extensive sulfide fractionation.

4.5 Implications for the generation of copper-rich fluids in arc magmatic systems

The abundance of Cu and other chalcophile elements in silicate melts is strongly influenced by sulfide saturation and the exsolution of volatiles during differentiation (Edmonds et al., 2018; Kiseeva et al., 2017). The relative importance of these two processes controls whether chalcophile elements are

563 sequestered in cumulates or transferred to upper-crustal reservoirs in hydrous fluids. Our modelling
564 (Fig. 7) indicates that sulfide saturation is nearly ubiquitous in calc-alkaline arc magmas as they evolve,
565 even under oxidised and hydrous conditions. Cooling, FeO depletion, and increasing melt
566 polymerisation act together to lower SCSS, promoting sulfide precipitation.

567 Because lower or mid-crustal sulfide saturation tends to scavenge Cu, magmas are rarely able
568 to accumulate large Cu inventories. Instead, Cu-rich ore fluids are more plausibly generated by the
569 interaction of later fluids with sulfide-bearing cumulates. Sulfides formed during differentiation may
570 be resorbed during volatile exsolution, as documented in Holuhraun, Iceland, where initial saturation
571 was followed by partial dissolution during sulfur degassing (Nicholson et al., 2024). Similar processes
572 are recognised in collisional arc settings, where volatile-rich fluids can leach and remobilise Cu from
573 pre-existing cumulates (Xia et al., 2023). In other cases, partial melting or rejuvenation of sulfide-rich
574 cumulates may liberate Cu to ascending melts or fluids, providing an additional source of metal in
575 porphyry systems (Heinrich and Connolly, 2022; Zhang et al., 2022).

576 The efficiency of Cu transfer is further enhanced once volatile saturation is reached, particularly
577 in the presence of Cl-rich fluids. Experiments and models demonstrate high fluid/melt partition
578 coefficients for Cu in saline fluids, with Cu-Cl complexes dominating transport (Blundy et al., 2015;
579 Yuan et al., 2025; Zajacz et al., 2017). These studies emphasise that brines are far more effective than
580 vapours or melts at scavenging Cu, and that the timing and composition of volatile exsolution strongly
581 influences porphyry fertility.

582 Taken together, the experimental and natural observations suggest that the occurrence of Cu -
583 (± Au) porphyry deposits is governed less by the capacity of magmas to remain Cu-rich, and more by
584 the architecture and evolution of the cumulate pile, the timing and depth of volatile saturation, and the
585 efficiency of Cl-rich fluids in mobilising metals. The co-precipitation of magnetite and sulfide in calc-
586 alkaline systems should therefore be regarded as a secondary rather than principal causative effect. The
587 SCSS depends primarily on melt composition, temperature, and the activity of S^{2-}, and not, as discussed
588 above (Figs 6 and 7) greatly on the fO_2. Even in oxidised magmas, sulfide fractionation remains

589 inevitable, underscoring that Cu enrichment in ore-forming fluids reflects the remobilisation of
590 previously sequestered sulfide rather than extraction from sulfide-undersaturated melts.

591 5. Conclusions

592 We have determined sulfide ($\log C_{S^{2-}}$) and sulfate ($\log C_{S^{6+}}$) capacities, in a wide range of silicate
593 melts at 1 atmosphere pressure and temperatures of 1050 to 1250°C. The data complement and extend
594 existing datasets (Boulliung and Wood, 2022, 2023; O'Neill and Mavrogenes 2002, 2022) which
595 provide analogous measurements at 1200 to 1500°C at 1 atmosphere. Extrapolating earlier sulfide
596 capacity models from 1200 to 1050°C is quite successful at reproducing our data, but sulfate models
597 significantly overestimate sulfate capacities at 1050°C. This means that S^{2-} is significantly more stable
598 at 1050°C than previously believed and that the temperature effect on the S^{6+}/S^{2-} ratio is much larger
599 than previously suggested. Our experiments show that the S^{2-}-S^{6+} crossover moves by ~+0.6 $\log fO_2$
600 units relative to the FMQ buffer between 1200 and 1050°C, nearly independent of melt composition.
601 S^{2-} is thus stabilised to progressively higher oxygen fugacities, relative to FMQ, as temperature declines.
602 Our observed temperature dependence of oxidation state at temperatures below 1200°C is several times
603 that calculated from the earlier models (O'Neill and Mavrogenes, 2022; Boulliung and Wood, 2023),
604 both of which underestimate sulfide stability at crustal conditions, but converges with them at
605 temperatures ≥1200°C.

606 An important consequence of the increased stability of sulfide in low temperature melts (<
607 1100ºC) is that it explains the observations of Matjuschkin et al., (2016) who found the field of S^{6+}
608 stability markedly reduced at 1.0 - 1.5GPa and 850-950°C relative to results at 0.2GPa and 1050°C.
609 This shift, ascribed by Matjuschkin et al. (2016) to a strong pressure effect on S speciation, is almost
610 entirely due to the effect of low temperatures rather than high pressures, as shown in Fig. 5b. Further,
611 it also indicates that our equations can be extrapolated to lower temperatures (~900°C).

612 Interaction between S and Fe oxidation states means that during ascent and cooling of melts
613 electrons are transferred from Fe^{2+} to S^{6+}, thereby increasing Fe^{3+}/Fe^{2+} and S^{2-}/S^{6+}. This process of self-

oxidation during ascent (Fig. 6), means that fO_2 may increase by +2 to +3 log units relative to FMQ before fluid saturation occurs, and S^{2-} becomes stable at relatively high fO_2. The extent of oxidation is governed jointly by the initial melt fO_2 and total sulfur content (Fig 7).

Progressive reduction of sulfur and oxidation of iron during ascent may be an important factor contributing to the observation that arc magmas are systematically more oxidised than MORB. In MORB, high eruption temperatures (>1200°C) and low initial fO_2 favour S^{2-}, limiting Fe-S redox exchange, whereas cooler S-rich arc magmas promote internal oxidation during crustal differentiation.

The enhanced low temperature stability of S^{2-} also means that sulfide saturation persists during differentiation of arc magmas, even under oxidising and hydrous conditions. This behaviour accounts for the widespread occurrence of sulfides in oxidised arc magmas and indicates that Cu-rich fluids should derive from remobilisation of cumulate sulfides rather than from sulfide-undersaturated melts.

Acknowledgements

This research was funded by UKRI grant *EP/X031063/1* "VulcansFluids" awarded to BJW. The authors are grateful to Andrew Matzen for help with EPMA analyses. We also thank James King, David Beer, and Zheyu (Jerry) Tian for laboratory support, and Elena Melekhova for helpful discussions.

References

Aiuppa, A., Moussallam, Y., 2024. Hydrogen and hydrogen sulphide in volcanic gases: abundance, processes, and atmospheric fluxes. Comptes Rendus. Géoscience 356, 1-23. https://doi.org/10.5802/crgeos.235

Ariskin, A.A., Danyushevsky, L.V., Bychkov, K.A., McNeill, A.W., Barmina, G.S., Nikolaev, G.S., 2013. Modeling Solubility of Fe-Ni Sulfides in Basaltic Magmas: The Effect of Nickel. Economic Geology 108, 1983-2003. https://doi.org/10.2113/econgeo.108.8.1983

636 Berry, A.J., Stewart, G.A., O'Neill, H.S.C., Mallmann, G., Mosselmans, J.F.W., 2018. A re-assessment
637 of the oxidation state of iron in MORB glasses. Earth and Planetary Science Letters 483, 114–
638 123. https://doi.org/10.1016/J.EPSL.2017.11.032
639 Blundy, J., Mavrogenes, J., Tattitch, B., Sparks, S., Gilmer, A., 2015. Generation of porphyry copper
640 deposits by gas–brine reaction in volcanic arcs. Nature Geosci 8, 235–240.
641 https://doi.org/10.1038/ngeo2351
642 Borisov, A., Jones, J.H., 1999. An evaluation of Re, as an alternative to Pt, for the 1 bar loop
643 technique; an experimental study at 1400 degrees C. American Mineralogist 84, 1528–1534.
644 https://doi.org/10.2138/am-1999-1006
645 Botcharnikov, R., Linnen L., R., Wilke, M., Holtz, F., Jugo J., P., Berndt, J., 2010. High gold
646 concentrations in sulphide-bearing magma under oxidizing conditions. Nature Geoscience 4,
647 112–112. https://doi.org/10.1038/ngeo1042
648 Boulliung, J., Wood, B.J., 2023. Sulfur oxidation state and solubility in silicate melts. Contrib Mineral
649 Petrol 178, 56. https://doi.org/10.1007/s00410-023-02033-9
650 Boulliung, J., Wood, B.J., 2022. SO2 solubility and degassing behavior in silicate melts. Geochimica
651 et Cosmochimica Acta 336, 150–164. https://doi.org/10.1016/j.gca.2022.08.032
652 Brounce, M., Stolper, E., Eiler, J., 2017. Redox variations in Mauna Kea lavas, the oxygen fugacity of
653 the Hawaiian plume, and the role of volcanic gases in Earth's oxygenation. Proceedings of the
654 National Academy of Sciences of the United States of America 114, 8997–9002.
655 https://doi.org/10.1073/pnas.1619527114
656 Brounce, M.N., Kelley, K.A., Cottrell, E., 2014. Variations in Fe3+/∑Fe of Mariana Arc Basalts and
657 Mantle Wedge fO2. Journal of Petrology 55, 2513–2536.
658 https://doi.org/10.1093/PETROLOGY/EGU065
659 Burgisser, A., Scaillet, B., 2007. Redox evolution of a degassing magma rising to the surface. Nature
660 445, 194–197. https://doi.org/10.1038/nature05509
661 Carroll, M.R., Rutherford, Malcolm. J., 1987. The Stability of Igneous Anhydrite: Experimental
662 Results and Implications for Sulfur Behavior in the 1982 El Chichon Trachyandesite and

663 Other Evolved Magmas. Journal of Petrology 28, 781–801.
664 https://doi.org/10.1093/petrology/28.5.781
665 Chase, M.W., National Institute of Standards and Technology, 1998. NIST-JANAF thermochemical
666 tables, 4th ed. ed, Journal of physical and chemical reference data. Monograph ; no. 9.
667 American Chemical Society, Washington, DC.
668 Chen, K., Tang, M., Lee, C.-T.A., Wang, Z., Zou, Z., Hu, Z., Liu, Y., 2020. Sulfide-bearing cumulates
669 in deep continental arcs: The missing copper reservoir. Earth and Planetary Science Letters
670 531, 115971. https://doi.org/10.1016/j.epsl.2019.115971
671 Clemente, B., Scaillet, B., Pichavant, M., 2004. The Solubility of Sulphur in Hydrous Rhyolitic Melts.
672 Journal of Petrology 45, 2171–2196. https://doi.org/10.1093/petrology/egh052
673 Cox, D., Watt, S.F.L., Jenner, F.E., Hastie, A.R., Hammond, S.J., 2019. Chalcophile element
674 processing beneath a continental arc stratovolcano. Earth and Planetary Science Letters 522,
675 1–11. https://doi.org/10.1016/j.epsl.2019.06.017
676 Edmonds, M., Mather, T.A., Liu, E.J., 2018. A distinct metal fingerprint in arc volcanic emissions.
677 Nature Geoscience 2018 11:10 11, 790–794. https://doi.org/10.1038/s41561-018-0214-5
678 Evans, K.-A., Tomkins, A.-G., 2011. The relationship between subduction zone redox budget and arc
679 magma fertility. Earth and Planetary Science Letters 308, 401–409.
680 https://doi.org/10.1016/j.epsl.2011.06.009
681 Fincham, C.J.B., Richardson, F.D., 1954. The behaviour of sulphur in silicate and aluminate melts.
682 Proceedings of the Royal Society of London. Series A. Mathematical and Physical Sciences
683 223, 40–62. https://doi.org/10.1098/rspa.1954.0099
684 Fortin, M.-A., Riddle, J., Desjardins-Langlais, Y., Baker, D.R., 2015. The effect of water on the sulfur
685 concentration at sulfide saturation (SCSS) in natural melts. Geochimica et Cosmochimica
686 Acta 160, 100–116. https://doi.org/10.1016/j.gca.2015.03.022
687 Friedman, J.H., Hastie, T., Tibshirani, R., 2010. Regularization Paths for Generalized Linear Models
688 via Coordinate Descent. Journal of Statistical Software 33, 1–22.
689 https://doi.org/10.18637/jss.v033.i01

690 Gaillard, F., Scaillet, B., Pichavant, M., Iacono-Marziano, G., 2015. The redox geodynamics linking
691 basalts and their mantle sources through space and time. Chemical Geology 418, 217–233.
692 https://doi.org/10.1016/j.chemgeo.2015.07.030
693 Georgatou, A., Chiaradia, M., Rezeau, H., Wälle, M., 2018. Magmatic sulphides in Quaternary
694 Ecuadorian arc magmas. Lithos 296–299, 580–599.
695 https://doi.org/10.1016/j.lithos.2017.11.019
696 Grove, T.L., 1982. Use of FePt alloys to eliminate the iron loss problem in 1 atmosphere gas mixing
697 experiments: Theoretical and practical considerations. Contr. Mineral. and Petrol. 78, 298–
698 304. https://doi.org/10.1007/BF00398924
699 Heinrich, C.A., Connolly, J.A.D., 2022. Physical transport of magmatic sulfides promotes copper
700 enrichment in hydrothermal ore fluids. Geology 50, 1101–1105.
701 https://doi.org/10.1130/G50138.1
702 Hughes, E.C., Liggins, P., Saper, L., Stolper, E.M., 2024. The effects of oxygen fugacity and sulfur on
703 the pressure of vapor-saturation of magma. American Mineralogist 109, 422–438.
704 https://doi.org/10.2138/am-2022-8739
705 Humphreys, M.C.S., Blundy, J., Sparks, S., 2006. Magma Evolution and Open-System Processes at
706 Shiveluch Volcano: Insights from Phenocryst Zoning. J Petrology 47, 2303–2334.
707 https://doi.org/10.1093/petrology/egl045
708 Jenner, F.E., O'Neill, H.S.C., 2012. Major and trace analysis of basaltic glasses by laser-ablation ICP-
709 MS. Geochemistry, Geophysics, Geosystems 13. https://doi.org/10.1029/2011GC003890
710 Jenner, F.E., O'Neill, H.ST.C., Arculus, R.J., Mavrogenes, J.A., 2010. The Magnetite Crisis in the
711 Evolution of Arc-related Magmas and the Initial Concentration of Au, Ag and Cu. Journal of
712 Petrology 51, 2445–2464. https://doi.org/10.1093/petrology/egq063
713 Jochum, K.P., Nohl, U., Herwig, K., Lammel, E., Stoll, B., Hofmann, A.W., 2007. GeoReM: A New
714 Geochemical Database for Reference Materials and Isotopic Standards. Geostandards and
715 Geoanalytical Research 29, 333–338. https://doi.org/10.1111/j.1751-908x.2005.tb00904.x
716 Jugo, P.J., Wilke, M., Botcharnikov, R.E., 2010. Sulfur K-edge XANES analysis of natural and
717 synthetic basaltic glasses: Implications for S speciation and S content as function of oxygen

718 fugacity. Geochimica et Cosmochimica Acta 74, 5926–5938.
719 https://doi.org/10.1016/J.GCA.2010.07.022
720 Kelley, K.A., Plank, T., Newman, S., Stolper, E.M., Grove, T.L., Parman, S., Hauri, E.H., 2010.
721 Mantle Melting as a Function of Water Content beneath the Mariana Arc. Journal of Petrology
722 51, 1711–1738. https://doi.org/10.1093/petrology/egq036
723 Kiseeva, E.S., Fonseca, R.O.C., Smythe, D.J., 2017. Chalcophile Elements and Sulfides in the Upper
724 Mantle. Elements 13, 111–116. https://doi.org/10.2113/gselements.13.2.111
725 Kleinsasser, J.M., Konecke, B.A., Simon, A.C., Northrup, P., Lanzirotti, A., Newville, M., Borca, C.,
726 Huthwelker, T., Holtz, F., 2024. Sulfur speciation in dacitic melts using X-ray absorption
727 near-edge structure spectroscopy of the S K-edge (S-XANES): Consideration of radiation-
728 induced changes and the implications for sulfur in natural arc systems. American
729 Mineralogist. https://doi.org/10.2138/am-2022-8833
730 Kress, V.C., 1997. Thermochemistry of sulfide liquids. I. the system O-S-Fe at 1 bar. Contrib Mineral
731 Petrol 127, 176–186. https://doi.org/10.1007/s004100050274
732 Kress, V.C., Carmichael, I.S.E., 1991. The compressibility of silicate liquids containing Fe2O3 and
733 the effect of composition, temperature, oxygen fugacity and pressure on their redox states.
734 Contributions to Mineralogy and Petrology 108, 82–92. https://doi.org/10.1007/BF00307328
735 Lee, C.-T.A., Luffi, P., Le Roux, V., Dasgupta, R., Albaréde, F., Leeman, W.P., 2010. The redox state
736 of arc mantle using Zn/Fe systematics. Nature 468, 681–5.
737 https://doi.org/10.1038/nature09617
738 Lerner, A.H., Muth, M.J., Wallace, P.J., Lanzirotti, A., Newville, M., Gaetani, G.A., Chowdhury, P.,
739 Dasgupta, R., 2021. Improving the reliability of Fe- and S-XANES measurements in silicate
740 glasses: Correcting beam damage and identifying Fe-oxide nanolites in hydrous and
741 anhydrous melt inclusions. Chemical Geology 586, 120610–120610.
742 https://doi.org/10.1016/J.CHEMGEO.2021.120610
743 Lesne, P., Scaillet, B., Pichavant, M., 2015. The solubility of sulfur in hydrous basaltic melts.
744 Chemical Geology 418, 104–116. https://doi.org/10.1016/j.chemgeo.2015.03.025

745 Luhr, J.F., 1990. Experimental phase relations of water- and sulfur- saturated arc magmas and the
746 1982 eruptions of El Chichon volcano. Journal of Petrology 31, 1071–1114.
747 https://doi.org/10.1180/minmag.1960.032.251.13
748 Marxer, F., Ulmer, P., Müntener, O., 2023. Ascent-driven differentiation: a mechanism to keep arc
749 magmas metaluminous? Contrib Mineral Petrol 178, 51. https://doi.org/10.1007/s00410-023-
750 02035-7
751 Matjuschkin, V., Blundy, J.D., Brooker, R.A., 2016. The effect of pressure on sulphur speciation in
752 mid- to deep-crustal arc magmas and implications for the formation of porphyry copper
753 deposits. Contributions to Mineralogy and Petrology 171. https://doi.org/10.1007/s00410-
754 016-1274-4
755 Métrich, N., Berry, A.J., O'Neill, H.S.C., Susini, J., 2009. The oxidation state of sulfur in synthetic
756 and natural glasses determined by X-ray absorption spectroscopy. Geochimica et
757 Cosmochimica Acta 73, 2382–2399. https://doi.org/10.1016/j.gca.2009.01.025
758 Muth, M.J., Cottrell, E., 2025. The effect of pressure on sulfur valence state in mafic silicate melts.
759 Earth and Planetary Science Letters 668, 119562. https://doi.org/10.1016/j.epsl.2025.119562
760 Muth, M.J., Wallace, P.J., 2021. Slab-derived sulfate generates oxidized basaltic magmas in the
761 southern Cascade arc (California, USA). Geology 49, 1177–1181.
762 https://doi.org/10.1130/G48759.1
763 Nash, W.M., Smythe, D.J., Wood, B.J., 2019. Compositional and temperature effects on sulfur
764 speciation and solubility in silicate melts. Earth and Planetary Science Letters 507, 187–198.
765 https://doi.org/10.1016/j.epsl.2018.12.006
766 Nicholson, E.J., Wieser, P.E., Hartley, M.E., Jenner, F.E., Kunz, B.E., Ilyinskaya, E., Thordarson, T.,
767 Edmonds, M., 2024. Sulfide saturation and resorption modulates sulfur and metal availability
768 during the 2014–15 Holuhraun eruption, Iceland. Commun Earth Environ 5, 1–19.
769 https://doi.org/10.1038/s43247-024-01249-2
770 O'Neill, H.St.C., 2021. The Thermodynamic Controls on Sulfide Saturation in Silicate Melts with
771 Application to Ocean Floor Basalts, in: Magma Redox Geochemistry, Geophysical
772 Monograph Series. American Geophysical Union, pp. 177–213.

O'Neill, H.St.C., Mavrogenes, J.A., 2022. The sulfate capacities of silicate melts. Geochimica et Cosmochimica Acta 334, 368–382. https://doi.org/10.1016/j.gca.2022.06.020

O'Neill, H.St.C., Mavrogenes, J.A., 2002. The Sulfide Capacity and the Sulfur Content at Sulfide Saturation of Silicate Melts at 1400°C and 1 bar. Journal of Petrology 43, 1049–1087. https://doi.org/10.1093/petrology/43.6.1049

Oppenheimer, C., Scaillet, B., Martin, R.S., 2011. Sulfur Degassing From Volcanoes: Source Conditions, Surveillance, Plume Chemistry and Earth System Impacts. Reviews in Mineralogy and Geochemistry 73, 363–421. https://doi.org/10.2138/rmg.2011.73.13

Richards, J.P., 2015. The oxidation state, and sulfur and Cu contents of arc magmas: implications for metallogeny. Lithos, Geochemistry and Earth Systems–A Special Issue in Memory of Robert Kerrich 233, 27–45. https://doi.org/10.1016/j.lithos.2014.12.011

Riel, N., Kaus, B.J.P., Green, E.C.R., Berlie, N., 2022. MAGEMin, an Efficient Gibbs Energy Minimizer: Application to Igneous Systems. Geochemistry, Geophysics, Geosystems 23, e2022GC010427. https://doi.org/10.1029/2022GC010427

Rowe, M.C., Kent, A.J.R., Nielsen, R.L., 2009. Subduction Influence on Oxygen Fugacity and Trace and Volatile Elements in Basalts Across the Cascade Volcanic Arc. J Petrology 50, 61–91. https://doi.org/10.1093/petrology/egn072

Ruscitto, D.M., Wallace, P.J., Johnson, E.R., Kent, A.J.R., Bindeman, I.N., 2010. Volatile contents of mafic magmas from cinder cones in the Central Oregon High Cascades: Implications for magma formation and mantle conditions in a hot arc. Earth and Planetary Science Letters 298, 153–161. https://doi.org/10.1016/j.epsl.2010.07.037

Saper, L.M., Brounce, M., Woelki, D., Cao, R., Bromiley, G., 2024. Variable oxidizing capacity of slab-derived fluids: Insights from Fe and S speciation in glasses from the Troodos Ophiolite. Earth and Planetary Science Letters 627, 118560. https://doi.org/10.1016/j.epsl.2023.118560

Shaw, A.M., Hauri, E.H., Fischer, T.P., Hilton, D.R., Kelley, K.A., 2008. Hydrogen isotopes in Mariana arc melt inclusions: Implications for subduction dehydration and the deep-Earth water cycle. Earth and Planetary Science Letters 275, 138–145. https://doi.org/10.1016/j.epsl.2008.08.015

Sillitoe, R.H., 2010. Porphyry Copper Systems*. Economic Geology 105, 3–41. https://doi.org/10.2113/gsecongeo.105.1.3

Smythe, D.J., Wood, B.J., Kiseeva, E.S., 2017. The S content of silicate melts at sulfide saturation: New experiments and a model incorporating the effects of sulfide composition. American Mineralogist 102, 795–803. https://doi.org/10.2138/am-2017-5800CCBY

Sugawara, T., 1999. Experimental techniques to minimize Fe and Na losses in one atmosphere gas mixing furnace. Journal of Mineralogy, Petrology and Economic Geology 94, 425–441. https://doi.org/10.2465/ganko.94.425

Taracsák, Z., Neave, D.A., Beaudry, P., Gunnarsson-Robin, J., Burgess, R., Edmonds, M., Halldórsson, S.A., Longpré, M.-A., Ono, S., Ranta, E., Stefánsson, A., Turchyn, A.V., Eimf, Hartley, M.E., 2021. Instrumental mass fractionation during sulfur isotope analysis by secondary ion mass spectrometry in natural and synthetic glasses. Chemical Geology 578, 120318. https://doi.org/10.1016/j.chemgeo.2021.120318

Ulmer, P., Kaegi, R., Müntener, O., 2018. Experimentally Derived Intermediate to Silica-rich Arc Magmas by Fractional and Equilibrium Crystallization at 1·0 GPa: an Evaluation of Phase Relationships, Compositions, Liquid Lines of Descent and Oxygen Fugacity. Journal of Petrology 59, 11–58. https://doi.org/10.1093/PETROLOGY/EGY017

Wallace, P.J., 2005. Volatiles in subduction zone magmas: concentrations and fluxes based on melt inclusion and volcanic gas data. Journal of Volcanology and Geothermal Research, Energy and Mass Fluxes in Volcanic Arcs 140, 217–240. https://doi.org/10.1016/j.jvolgeores.2004.07.023

White, W.B., Johnson, S.M., Dantzig, G.B., 1958. Chemical Equilibrium in Complex Mixtures. J. Chem. Phys. 28, 751–755. https://doi.org/10.1063/1.1744264

Wilke, M., Jugo, P.J., Klimm, K., Susini, J., Botcharnikov, R., Kohn, S.C., Janousch, M., 2008. The origin of S4+ detected in silicate glasses by XANES. American Mineralogist 93, 235–240. https://doi.org/10.2138/am.2008.2765

Wood, B.J., Nicholls, J., 1978. The thermodynamic properties of reciprocal solid solutions. Contr. Mineral. and Petrol. 66, 389–400. https://doi.org/10.1007/BF00403424

Xia, W., Wang, R., Jenner, F., 2023. Sulfide resorption contributes to porphyry deposit formation in collisional settings. Ore Geology Reviews 163, 105804. https://doi.org/10.1016/j.oregeorev.2023.105804

Yuan, S., Williams-Jones, A.E., Bodnar, R.J., Zhao, P., Zajacz, Z., Chou, I.-M., Mao, J., 2025. The role of magma differentiation in optimizing the fluid-assisted extraction of copper to generate large porphyry-type deposits. Science Advances 11, eadr8464. https://doi.org/10.1126/sciadv.adr8464

Zajacz, Z., Candela, P.A., Piccoli, P.M., 2017. The partitioning of Cu, Au and Mo between liquid and vapor at magmatic temperatures and its implications for the genesis of magmatic-hydrothermal ore deposits. Geochimica et Cosmochimica Acta 207, 81–101. https://doi.org/10.1016/j.gca.2017.03.015

Zhang, J., Chang, J., Wang, R., Audétat, A., 2022. Can Post-Subduction Porphyry Cu Magmas Form by Partial Melting of Typical Lower Crustal Amphibole-Rich Cumulates? Petrographic and Experimental Constraints from Samples of the Kohistan and Gangdese Arc Roots. J Petrology 63, egac101. https://doi.org/10.1093/petrology/egac101

Table 1. Major element compositions of starting materials used to test sulfide and sulfate solubilities

Composition	SiO_2	TiO_2	Al_2O_3	FeOtot	MnO	MgO	CaO	Na_2O	K_2O	Total
Icelandic Basalt[a]	49.6	0.92	14.6	9.0	0.17	8.7	12.4	2.3	0.21	98.2
Nepheline Basanite[a]	43.8	2.3	10.9	11.52	0.18	13.1	9.4	3.9	1.9	98.4
AJ99 Basanite[a]	44.4	3.1	14.8	6.3	-	6.6	10.2	4.0	1.6	98.6
High-Mg Basalt[a]	45.4	4.4	10.4	7.2	0.17	14.1	11.4	1.1	0.20	98.6
T-Basalt[a]	47.0	3.3	16.4	10.3	0.21	4.3	9.4	4.7	1.9	98.7
Phonolite[a]	55.2	0.34	21.9	2.8	0.26	0.1	1.8	8.2	8.6	99.5
T-Basaltic Andesite[b]	56.3	2.2	23.3	3.2	1.1	2.2	4.7	2.7	3.7	99.4
T-Andesite[b]	57.9	3.7	25.2	1.6	0.20	0.2	1.9	3.6	5.4	99.8
Foidite[b]	38.2	2.7	18.1	2.8	0.25	0.2	1.5	17.9	15.9	97.6
Nephelenite[a]	41.7	2.7	14.2	9.9	2.5	8.0	13.9	4.0	3.2	99.9
T-Phonolite[a]	53.3	1.5	22.9	4.4	-	1.9	4.8	7.8	3.6	100.4
Fe-Free T-Phonolite[a]	58.2	1.9	21.6	-	0.11	2.0	5.0	7.3	3.0	99.0
Basaltic Andesite[a]	53.9	0.61	14.6	6.4	-	9.4	9.9	2.8	1.3	99.0
DAC[c]	64.2	0.70	16.8	5.1	0.10	2.1	5.6	4.0	1.4	100.0

[a] Boulliung and Wood 2022, 2023
[b] Synthesized for this study
[c] Nash et al. 2019

845

Table 2. Experimental conditions, compositions of experimental products (in wt.%), and calculated sulfide capacities from equilibration experiments. Uncertainties (2 s.d.) are given in parentheses.

Sample	T (°C)	t (h)	XSO_2	XCO	XCO_2	logfO_2	logfS_2	SiO_2		TiO_2		Al_2O_3		FeO		MnO		MgO		CaO		Na_2O		K_2O		Total	S (ppm)		logC_{S2-}	
AJ99 Basanite	1050	120	0.23	0.44	0.33	-11.2	-1.0	53.0	(1.5)	2.6	(0.8)	9.8	(5.3)	9.7	(2.4)	-	-	7.4	(1.5)	12.7	(3.4)	2.7	(1.1)	1.2	(0.5)	98.9	748	(338)	-6.2	(0.2)
DAC	1050	120	0.23	0.44	0.33	-11.2	-1.0	72.3	(2.4)	0.71	(0.10)	12.9	(1.5)	2.9	(0.7)	0.10	(0.03)	0.77	(2.43)	3.9	(1.7)	4.5	(0.5)	2.3	(0.3)	100.8	191	(58)	-6.8	(0.2)
Fe-Free T-Phonolite	1050	120	0.23	0.44	0.33	-11.2	-1.0	62.2	(2.1)	1.2	(0.6)	22.5	(1.9)	0.08	(0.05)	0.12	(0.05)	0.92	(2.14)	5.2	(2.0)	7.3	(0.4)	1.6	(1.0)	101.3	86	(23)	-7.2	(0.1)
Foidite	1050	120	0.23	0.44	0.33	-11.2	-1.0	56.7	(1.6)	3.4	(0.6)	25.4	(1.1)	2.0	(0.4)	0.23	(0.09)	0.31	(1.65)	1.7	(0.8)	9.9	(1.3)	2.0	(0.2)	102.0	533	(212)	-6.4	(0.2)
Icelandic Basalt	1050	120	0.23	0.44	0.33	-11.2	-1.0	52.0	(0.8)	0.74	0.23	16.1	(2.3)	6.9	(0.6)	0.17	(0.03)	8.6	(0.8)	13.3	(1.7)	2.2	(0.6)	0.33	(0.16)	100.6	300	(66)	-6.6	(0.1)
Nephelenite	1050	120	0.23	0.44	0.33	-11.2	-1.0	48.3	(3.4)	1.6	(1.0)	19.0	(8.1)	4.7	(2.2)	1.9	(0.9)	6.8	(3.4)	16.9	(2.3)	1.8	(0.9)	0.05	(0.02)	101.0	292	(53)	-6.6	(0.1)
Phonolite	1050	120	0.23	0.44	0.33	-11.2	-1.0	55.7	(0.9)	0.34	(0.07)	24.3	(0.7)	2.9	(0.5)	0.32	(0.07)	0.18	(0.86)	1.8	(1.1)	8.3	(0.8)	6.5	(1.2)	100.6	1115	(603)	-6.1	(0.3)
T-Andesite	1050	120	0.23	0.44	0.33	-11.2	-1.0	59.9	(4.5)	4.0	(0.6)	26.1	(2.8)	0.78	(0.52)	0.14	(0.06)	0.20	(4.50)	0.57	1.04	3.9	(0.7)	5.6	(0.6)	101.2	696	(74)	-6.3	(0.1)
T-Basalt	1050	120	0.23	0.44	0.33	-11.2	-1.0	50.4	(2.4)	2.2	(0.6)	17.1	(6.8)	6.0	(2.0)	0.36	(0.12)	4.9	(2.4)	13.6	(4.3)	3.4	(1.5)	0.88	(0.30)	98.9	581	(189)	-6.3	(0.2)
T-Basaltic Andesite	1050	120	0.23	0.44	0.33	-11.2	-1.0	58.7	(3.3)	2.0	(0.5)	21.6	(2.3)	3.3	(0.8)	0.90	(0.14)	1.5	(3.3)	4.1	(1.9)	3.5	(0.4)	4.5	(1.1)	100.4	125	(62)	-7.0	(0.2)
T-Phonolite	1050	120	0.23	0.44	0.33	-11.2	-1.0	59.3	(1.7)	1.8	(0.1)	20.1	(0.8)	5.4	(1.1)	0.14	(0.04)	1.6	(1.7)	2.5	(0.6)	7.8	(0.3)	3.6	(0.3)	100.2	354	(71)	-6.6	(0.1)
AJ99 Basanite	1100	72	0.19	0.52	0.29	-11.2	-1.1	46.1	(1.3)	4.7	(0.7)	12.5	(0.2)	12.3	(1.0)	0.55	(0.04)	5.7	(1.3)	10.4	(0.4)	3.5	(0.1)	1.1	(0.1)	96.9	1765	(265)	-5.8	(0.1)
DAC	1100	72	0.19	0.52	0.29	-11.2	-1.1	68.5	(3.6)	0.64	0.11	15.3	(4.5)	3.1	(0.6)	0.13	(0.03)	1.4	(3.6)	4.8	(1.3)	4.4	(0.3)	2.0	(0.3)	100.7	219	(39)	-6.7	(0.1)
Fe-Free T-Phonolite	1100	72	0.19	0.52	0.29	-11.2	-1.1	58.8	(1.5)	1.6	(0.5)	22.4	(2.7)	0.12	(0.03)	0.13	(0.03)	1.6	(1.5)	5.1	(2.0)	8.3	(1.1)	2.9	(1.1)	100.9	374	(170)	-6.5	(0.2)
Foidite	1100	72	0.19	0.52	0.29	-11.2	-1.1	53.7	(0.8)	4.1	(0.2)	25.5	(0.4)	1.1	(0.3)	0.22	(0.07)	0.28	(0.79)	2.1	(0.4)	12.1	(0.4)	1.1	(0.0)	100.6	1291	(255)	-6.0	(0.1)
High Mg-Basalt	1100	72	0.19	0.52	0.29	-11.2	-1.1	47.5	(2.1)	3.9	(1.5)	8.8	(4.7)	7.8	(2.4)	0.21	(0.07)	12.3	(2.1)	16.8	(4.9)	1.5	(1.0)	0.34	(0.16)	99.0	659	(370)	-6.3	(0.3)
Nephelenite	1100	72	0.19	0.52	0.29	-11.2	-1.1	43.5	(0.7)	5.9	(1.7)	10.3	(1.2)	10.6	(1.3)	4.6	(0.6)	9.4	(0.7)	12.6	(2.8)	2.1	(0.5)	0.62	(0.25)	100.2	2678	(403)	-5.7	(0.1)
Nepheline Basanite	1100	72	0.19	0.52	0.29	-11.2	-1.1	53.0	(1.5)	5.6	(1.2)	13.2	(3.3)	6.7	(1.5)	0.29	(0.03)	7.4	(3.2)	10.1	(0.2)	2.7	(1.1)	1.1	(0.2)	95.3	923	(59)	-6.1	(0.0)
Phonolite	1100	72	0.19	0.52	0.29	-11.2	-1.1	55.4	(0.8)	0.30	(0.02)	23.7	(0.2)	2.9	(0.6)	0.28	(0.08)	0.15	(0.77)	2.1	(0.4)	7.7	(0.3)	6.5	(0.2)	99.8	2886	(1413)	-5.6	(0.2)
T-Andesite	1100	72	0.19	0.52	0.29	-11.2	-1.1	57.5	(3.0)	3.9	(0.7)	24.4	(2.1)	1.6	(0.7)	0.26	(0.09)	0.24	(3.02)	0.84	(0.99)	5.0	(0.5)	6.1	(0.6)	100.5	4632	(1135)	-5.4	(0.1)
T-Basaltic Andesite	1100	72	0.19	0.52	0.29	-11.2	-1.1	59.8	(0.9)	2.3	(0.1)	20.8	(1.1)	2.2	(0.4)	0.94	(0.09)	1.9	(0.9)	2.6	(0.6)	4.0	(0.2)	5.0	(0.3)	99.7	631	(101)	-6.3	(0.1)
T-Phonolite	1100	72	0.19	0.52	0.29	-11.2	-1.1	56.8	(2.3)	1.8	(0.2)	21.3	(1.0)	4.9	(1.0)	0.14	(0.04)	2.0	(2.3)	3.3	(1.1)	8.0	(0.5)	3.0	(0.4)	101.2	359	(92)	-6.5	(0.1)
AJ99 Basanite	1150	24	0.14	0.60	0.27	-11.2	-1.2	51.0	(0.6)	4.6	(0.1)	13.5	(0.2)	7.2	(0.4)	-	-	7.6	(0.6)	11.2	(0.2)	1.8	(0.2)	0.56	0.03	97.7	909	(144)	-6.1	(0.1)
DAC	1150	24	0.14	0.60	0.27	-11.2	-1.2	67.9	(0.8)	0.74	(0.06)	15.1	(1.0)	2.6	(0.4)	0.14	(0.04)	2.2	(0.8)	5.8	(0.3)	3.6	(0.3)	1.6	(0.1)	99.7	612	(289)	-6.2	(0.2)
Fe-Free T-Phonolite	1150	24	0.14	0.60	0.27	-11.2	-1.2	57.8	(1.5)	1.6	(0.8)	22.3	(3.2)	0.16	(0.05)	0.16	(0.06)	2.1	(1.5)	6.9	(2.2)	6.5	(0.8)	1.7	(0.8)	99.2	531	(347)	-6.3	(0.3)
Foidite	1150	24	0.14	0.60	0.27	-11.2	-1.2	58.6	(2.8)	3.4	(0.6)	25.0	(2.2)	0.56	(0.13)	0.13	(0.02)	0.15	(2.75)	1.4	(0.3)	10.2	(0.3)	1.7	(0.1)	101.2	1610	(432)	-5.8	(0.1)
High Mg-Basalt	1150	24	0.14	0.60	0.27	-11.2	-1.2	57.0	(3.8)	0.98	(0.61)	14.6	(5.9)	5.4	(1.0)	-	-	8.3	(3.8)	10.7	(1.7)	1.9	(0.3)	0.60	(0.19)	99.7	1016	(604)	-6.0	(0.3)
Icelandic Basalt	1150	24	0.14	0.60	0.27	-11.2	-1.2	54.3	(1.6)	1.0	(0.2)	16.7	(1.7)	4.3	(0.5)	0.16	(0.04)	8.2	(1.6)	12.6	(1.2)	2.1	(0.3)	0.59	(0.24)	100.0	734	(485)	-6.1	(0.3)
Nephelenite	1150	24	0.14	0.60	0.27	-11.2	-1.2	46.7	(0.5)	5.8	(0.4)	8.4	(0.5)	5.5	(0.8)	3.6	(0.2)	11.8	(0.5)	16.5	(0.6)	0.66	(0.11)	0.10	(0.02)	99.4	1483	(789)	-5.8	(0.3)
Phonolite	1150	24	0.14	0.60	0.27	-11.2	-1.2	56.2	(0.5)	0.32	(0.01)	24.2	(0.3)	1.9	(0.2)	0.29	(0.02)	0.16	(0.53)	2.2	(0.1)	7.8	(0.2)	6.2	(0.1)	99.6	2042	(833)	-5.7	(0.2)
T-Andesite	1150	24	0.14	0.60	0.27	-11.2	-1.2	58.0	(2.6)	3.7	(0.6)	23.8	(1.5)	1.5	(0.3)	0.18	(0.05)	0.29	(2.56)	3.0	(2.6)	4.8	(0.3)	4.5	(1.3)	100.7	4634	(1444)	-5.3	(0.2)
T-Basaltic Andesite	1150	24	0.14	0.60	0.27	-11.2	-1.2	57.3	(4.1)	2.5	(0.4)	23.3	(3.3)	2.2	(0.9)	1.1	(0.2)	2.7	(4.1)	3.8	(1.7)	3.0	(0.3)	3.4	(0.6)	99.6	2579	(413)	-5.6	(0.1)
T-Phonolite	1150	24	0.14	0.60	0.27	-11.2	-1.2	58.3	(1.7)	1.7	(0.1)	21.0	(0.7)	4.0	(0.5)	0.17	(0.06)	2.2	(1.7)	3.3	(0.5)	6.7	(0.3)	2.2	(0.1)	99.8	667	(277)	-6.2	(0.2)
AJ99 Basanite	1200	24	0.07	0.67	0.26	-11.2	-1.6	54.4	(0.5)	4.0	(0.1)	17.2	(0.3)	1.4	(0.1)	-	-	8.3	(0.5)	11.7	(0.1)	1.5	(0.1)	0.56	0.02	99.2	457	(50)	-6.2	(0.1)
Basaltic Andesite	1200	24	0.07	0.67	0.26	-11.2	-1.6	61.0	(0.5)	0.76	(0.08)	16.2	(0.3)	1.0	(0.32)	-	-	6.7	(0.5)	9.2	(0.4)	2.7	(0.2)	1.4	(0.1)	99.1	510	(93)	-6.1	(0.2)
DAC	1200	24	0.07	0.67	0.26	-11.2	-1.6	67.0	(2.6)	0.71	(0.04)	16.3	(1.8)	1.9	(0.3)	0.14	(0.03)	2.1	(2.6)	5.5	(0.8)	4.1	(0.3)	1.7	(0.1)	99.5	395	(152)	-6.2	(0.2)
Fe-Free T-Phonolite	1200	24	0.07	0.67	0.26	-11.2	-1.6	55.4	(0.7)	1.6	(0.0)	22.7	(0.3)	3.6	(0.2)	0.19	(0.02)	2.7	(0.7)	5.8	(0.2)	5.8	(0.3)	1.6	(0.0)	99.5	777	(126)	-5.9	(0.2)
Foidite	1200	24	0.07	0.67	0.26	-11.2	-1.6	58.9	(1.7)	3.5	(0.2)	23.7	(0.6)	0.46	(0.21)	0.14	(0.05)	0.19	(1.71)	2.5	(0.4)	5.8	(0.3)	4.6	(0.1)	101.6	1726	(45)	-5.6	(0.1)
High Mg-Basalt	1200	24	0.07	0.67	0.26	-11.2	-1.6	49.3	(0.4)	5.6	(0.0)	13.4	(0.1)	3.2	(0.1)	0.17	(0.03)	10.7	(0.4)	14.4	(0.1)	0.90	(0.09)	0.16	(0.02)	98.0	1184	(140)	-5.7	(0.1)
Icelandic Basalt	1200	24	0.07	0.67	0.26	-11.2	-1.6	56.2	(0.5)	1.1	(0.0)	15.5	(0.1)	3.4	(0.1)	0.19	(0.04)	8.9	(0.5)	13.1	(0.1)	1.3	(0.1)	0.33	(0.01)	100.2	863	(76)	-5.9	(0.1)
Nephelenite	1200	24	0.07	0.67	0.26	-11.2	-1.6	50.7	(0.3)	4.3	(0.0)	14.9	(0.1)	0.52	(0.05)	2.1	(0.1)	10.6	(0.3)	14.9	(0.1)	0.72	(0.10)	0.11	(0.02)	99.0	701	(82)	-6.0	(0.1)
Nepheline Basanite	1200	24	0.07	0.67	0.26	-11.2	-1.6	53.2	(0.6)	3.0	(0.0)	14.5	(0.1)	2.6	(0.2)	0.19	(0.03)	10.0	(0.6)	12.1	(0.1)	1.5	(0.1)	0.29	(0.02)	97.5	743	(164)	-5.9	(0.2)
Phonolite	1200	24	0.07	0.67	0.26	-11.2	-1.6	58.4	(1.3)	0.32	(0.04)	25.3	(0.8)	1.3	(0.2)	0.17	(0.03)	0.10	(1.35)	1.6	(0.2)	7.3	(0.2)	6.0	(0.1)	100.6	1175	(518)	-5.8	(0.3)
T-Andesite	1200	24	0.07	0.67	0.26	-11.2	-1.6	63.8	(2.9)	3.9	(0.2)	22.7	(3.8)	0.57	(0.17)	0.16	(0.06)	0.31	(2.87)	1.8	(0.2)	3.7	(0.3)	4.1	(0.3)	101.0	1995	(638)	-5.5	(0.2)
T-Basalt	1200	24	0.07	0.67	0.26	-11.2	-1.6	54.5	(0.4)	4.1	(0.0)	15.6	(0.1)	2.0	(0.0)	0.50	(0.04)	6.8	(0.4)	13.5	(0.1)	1.0	(0.1)	0.43	(0.01)	98.4	646	(78)	-6.0	(0.1)
T-Basaltic Andesite	1200	24	0.07	0.67	0.26	-11.2	-1.6	61.4	(0.5)	3.0	(0.2)	20.7	(0.3)	1.3	(0.2)	0.93	(0.09)	2.8	(0.5)	3.2	(0.2)	2.9	(0.1)	3.5	(0.1)	100.0	4769	(52)	-5.1	(0.1)
T-Phonolite	1200	24	0.07	0.67	0.26	-11.2	-1.6	58.8	(0.4)	1.7	(0.1)	21.5	(0.4)	0.10	(0.02)	0.14	(0.02)	2.5	(0.4)	6.5	(0.2)	6.5	(0.3)	2.1	(0.1)	99.8	295	(66)	-6.4	(0.2)

Table 3. Experimental conditions, compositions of experimental products (in wt.%), and calculated sulfate capacities from equilibration experiments. Uncertainties (2 s.d.) are given in parentheses.

Sample	T (°C)	t (h)	Xair	XSO_2	logfO_2	logfS_2	SiO_2		TiO_2		Al_2O_3		FeO		MnO		MgO		CaO		Na_2O		K_2O		Total	S (ppm)		logC_{S6+}	
Fe-free T-Phonolite	1048	120	0.38	0.62	-1.1	-19.2	61.1	(1.7)	2.1	(0.7)	22.3	(1.2)	0.11	(0.03)	0.16	(0.06)	1.5	(0.7)	2.2	(1.9)	7.3	(1.1)	4.1	(1.5)	101	273	(114)	9.7	(0.3)
Fe-free T-Phonolite	1050	120	0.38	0.62	-1.1	-19.1	60.6	(1.9)	1.7	(0.6)	21.9	(1.5)	0.08	(0.02)	0.10	(0.03)	0.90	(0.44)	2.6	(2.3)	6.1	(0.5)	3.7	(1.5)	98	350	(180)	9.7	(0.3)
Foidite	1048	120	0.38	0.62	-1.1	-19.2	55.3	(3.3)	3.8	(1.9)	24.4	(2.0)	2.9	(1.7)	0.08	(0.03)	0.06	(0.02)	0.2	(0.2)	9.3	(1.1)	4.9	(0.4)	101	539	(182)	10.0	(0.2)
Foidite	1050	120	0.38	0.62	-1.1	-19.1	49.0	(1.8)	3.4	(1.3)	23.6	(1.9)	3.5	(1.0)	0.19	(0.05)	0.16	(0.06)	0.41	(0.34)	4.5	(2.4)	14.6	(2.1)	99	461	(228)	9.9	(0.3)
Nephelenite	1048	120	0.38	0.62	-1.1	-19.2	65.3	(1.2)	1.3	(0.3)	18.9	(1.1)	2.3	(0.2)	0.66	(0.13)	1.4	(0.3)	2.6	(1.1)	4.3	(0.2)	4.3	(0.8)	101	412	(150)	9.8	(0.3)
Nephelenite	1050	120	0.38	0.62	-1.1	-19.1	62.4	(1.8)	2.0	(0.4)	17.8	(0.9)	2.8	(0.7)	0.71	(0.12)	1.9	(0.3)	2.9	(0.4)	5.3	(0.4)	4.6	(0.2)	100	424	(166)	9.8	(0.3)
Phonolite	1048	120	0.38	0.62	-1.1	-19.2	56.7	(2.1)	0.31	(0.03)	24.3	(1.1)	2.4	(1.8)	0.29	(0.26)	0.13	(0.09)	1.6	(0.4)	7.5	(0.5)	6.7	(0.3)	100	2578	(1457)	10.6	(0.3)
T-Andesite	1048	120	0.38	0.62	-1.1	-19.2	57.9	(4.0)	3.5	(0.9)	23.5	(2.3)	2.0	(1.0)	0.20	(0.08)	0.18	(0.07)	3.8	(2.2)	4.5	(0.7)	3.9	(1.5)	99	193	(80)	9.5	(0.3)
T-Andesite	1050	120	0.38	0.62	-1.1	-19.1	57.7	(3.4)	4.0	(1.0)	24.1	(2.8)	2.3	(1.4)	0.24	(0.11)	0.25	(0.13)	2.8	(1.9)	4.2	(0.5)	4.4	(1.4)	100	141	(40)	9.4	(0.2)
T-Basaltic Andesite	1048	120	0.38	0.62	-1.1	-19.2	56.1	(1.9)	2.4	(0.5)	23.0	(0.8)	3.9	(1.3)	1.08	(0.25)	1.8	(1.0)	6.2	(1.8)	2.8	(0.3)	2.4	(0.6)	100	103	(64)	10.3	(0.4)
T-Basalt	1048	120	0.38	0.62	-1.1	-19.2	59.7	(3.4)	0.77	(0.47)	21.6	(2.0)	1.9	(0.7)	0.10	(0.02)	0.63	(0.33)	5.8	(2.4)	4.8	(0.7)	2.9	(1.3)	98	1250	(647)	10.3	(0.3)
T-Basalt	1050	120	0.38	0.62	-1.1	-19.1	46.9	(2.1)	2.1	(0.6)	17.3	(1.5)	9.0	(2.1)	0.29	(0.09)	4.6	(1.5)	12.4	(3.1)	3.7	(0.5)	1.0	(0.4)	98	774	(333)	10.1	(0.3)
T-Phonolite	1048	120	0.38	0.62	-1.1	-19.2	61.8	(2.7)	1.6	(0.4)	19.8	(1.1)	3.1	(1.7)	0.14	(0.09)	1.2	(0.7)	1.1	(0.7)	7.7	(1.0)	4.3	(0.6)	101	327	(148)	9.7	(0.3)
T-Phonolite	1050	120	0.38	0.62	-1.1	-19.1	61.5	(3.8)	1.8	(0.5)	18.7	(2.4)	4.2	(1.4)	0.11	(0.03)	1.3	(0.6)	2.5	(1.7)	6.5	(0.7)	3.7	(0.9)	100	311	(190)	9.7	(0.4)
AJ99 Basanite	1100	72	0.38	0.62	-1.1	-18.1	51.4	(1.4)	1.8	(0.9)	18.7	(5.1)	5.6	(0.8)	-	-	5.4	(2.4)	10.1	(1.8)	3.3	(0.1)	1.3	(0.7)	98	376	(188)	9.3	(0.3)
Basaltic Andesite	1100	72	0.38	0.62	-1.1	-18.1	57.5	(2.2)	0.6	(0.1)	13.3	(2.1)	5.7	(0.6)	-	-	9.2	(1.9)	8.5	(1.6)	2.6	(0.3)	1.5	(0.5)	99	640	(209)	9.5	(0.2)
Fe-free T-Phonolite	1100	72	0.38	0.62	-1.1	-18.1	60.7	(1.4)	1.8	(0.1)	22.4	(0.4)	0.08	(0.02)	0.10	(0.03)	1.7	(0.5)	3.6	(0.8)	7.1	(0.3)	3.1	(0.5)	101	366	(145)	9.3	(0.3)
Foidite	1100	72	0.38	0.62	-1.1	-18.1	56.1	(0.9)	3.6	(0.3)	24.8	(0.5)	2.3	(0.5)	0.08	(0.03)	0.06	(0.02)	0.27	(0.05)	7.5	(0.3)	6.1	(0.1)	101	1823	(760)	10.0	(0.3)
High-Mg Basalt	1100	72	0.38	0.62	-1.1	-18.1	53.9	(0.8)	2.5	(0.1)	14.1	(0.3)	6.3	(0.5)	0.18	(0.02)	6.6	(0.1)	9.2	(0.1)	3.1	(0.1)	1.6	(0.0)	98	3895	(816)	10.3	(0.2)
Nephelenite	1100	72	0.38	0.62	-1.1	-18.1	53.9	(0.6)	2.6	(0.1)	15.4	(0.3)	5.0	(0.2)	1.99	(0.09)	5.8	(0.2)	7.4	(0.2)	3.3	(0.2)	2.5	(0.1)	98	3273	(383)	10.2	(0.2)
Nepheline Basanite	1100	72	0.38	0.62	-1.1	-18.1	54.2	(4.4)	1.7	(0.1)	13.7	(1.2)	6.1	(1.1)	0.16	(0.04)	7.1	(2.6)	8.6	(3.1)	3.4	(0.8)	1.8	(0.6)	97	1222	(670)	9.8	(0.3)
Phonolite	1100	72	0.38	0.62	-1.1	-18.1	57.2	(1.2)	0.29	(0.04)	23.7	(0.6)	2.5	(0.6)	0.24	(0.11)	0.11	(0.04)	1.2	(0.5)	6.7	(0.4)	7.2	(0.3)	100	1733	(594)	9.9	(0.3)
T-Andesite	1100	72	0.38	0.62	-1.1	-18.1	57.9	(3.4)	3.7	(1.0)	24.3	(3.2)	2.0	(0.9)	0.28	(0.07)	0.26	(0.06)	1.5	(0.3)	4.2	(0.5)	5.8	(0.4)	100	325	(134)	9.2	(0.3)
T-Basalt	1100	72	0.38	0.62	-1.1	-18.1	56.7	(1.1)	1.7	(0.3)	18.0	(1.7)	4.1	(0.5)	0.26	(0.06)	3.3	(0.7)	6.0	(1.0)	4.2	(0.1)	3.7	(0.6)	98	1930	(518)	10.0	(0.2)
T-Basalt	1100	72	0.38	0.62	-1.1	-18.1	50.5	(1.3)	2.1	(0.1)	14.6	(0.5)	6.2	(0.4)	0.53	(0.07)	6.9	(0.7)	9.0	(0.8)	3.2	(0.2)	2.5	(0.3)	96	1708	(303)	9.9	(0.2)
T-Basaltic Andesite	1100	72	0.38	0.62	-1.1	-18.1	54.9	(1.8)	2.6	(0.8)	22.7	(1.6)	3.9	(1.2)	0.83	(0.19)	1.4	(0.5)	6.2	(1.9)	3.1	(0.1)	3.4	(0.7)	99	190	(84)	9.0	(0.3)
T-Phonolite	1100	72	0.38	0.62	-1.1	-18.1	58.5	(1.7)	1.6	(0.1)	20.5	(1.2)	4.4	(0.6)	0.14	(0.02)	2.0	(0.2)	3.8	(0.6)	7.3	(0.7)	3.0	(0.1)	101	168	(70)	8.9	(0.3)
AJ99 Basanite	1123	24	0.38	0.62	-1.1	-17.6	48.1	(0.3)	2.4	(0.0)	15.7	(0.1)	7.7	(0.1)	-	-	6.7	(0.0)	10.9	(0.1)	3.5	(0.1)	1.3	(0.0)	97	3291	(123)	10.0	(0.2)
Fe-free T-Phonolite	1123	24	0.38	0.62	-1.1	-17.6	58.4	(0.4)	1.8	(0.0)	21.5	(0.1)	0.15	(0.02)	0.13	(0.01)	2.0	(0.1)	5.0	(0.1)	7.0	(0.2)	2.9	(0.0)	99	483	(177)	9.2	(0.3)
Foidite	1123	24	0.38	0.62	-1.1	-17.6	53.4	(1.0)	3.7	(0.3)	25.3	(0.3)	3.0	(0.5)	0.16	(0.03)	0.13	0.01	0.4	(0.1)	10.3	(0.3)	4.0	(0.1)	101	888	(59)	9.4	(0.2)
Nephelenite	1123	24	0.38	0.62	-1.1	-17.6	62.4	(0.2)	1.6	(0.1)	15.5	(0.2)	3.6	(0.1)	1.5	(0.1)	3.4	(0.1)	4.7	(0.2)	4.0	(0.1)	3.0	(0.1)	100	1871	(338)	9.7	(0.2)
Phonolite	1123	24	0.38	0.62	-1.1	-17.6	45.6	(0.4)	3.6	(0.3)	11.4	(0.8)	9.2	(0.6)	0.18	(0.02)	11.2	(4.2)	12.4	(1.0)	1.8	(0.2)	0.53	(0.05)	97	3543	(438)	10.0	(0.2)
T-Andesite	1123	24	0.38	0.62	-1.1	-17.6	57.6	(3.4)	3.7	(0.7)	23.8	(2.3)	2.3	(0.7)	0.29	(0.12)	0.26	(0.08)	2.2	(2.1)	4.4	(0.3)	5.3	(1.2)	100	144	(27)	8.6	(0.2)
T-Basalt	1123	24	0.38	0.62	-1.1	-17.6	48.6	(0.3)	2.1	(0.0)	17.3	(0.2)	6.9	(0.1)	0.34	(0.02)	4.4	(0.1)	10.0	(0.0)	3.3	(0.2)	1.9	(0.0)	95	2636	(106)	9.9	(0.2)
T-Basaltic Andesite	1123	24	0.38	0.62	-1.1	-17.6	56.1	(1.7)	2.2	(0.5)	22.8	(1.5)	3.3	(1.1)	1.0	(0.4)	1.8	(1.0)	5.3	(2.4)	3.0	(0.7)	3.2	(1.0)	99	86	(26)	8.4	(0.2)
T-Phonolite	1123	24	0.38	0.62	-1.1	-17.6	57.7	(2.5)	2.2	(0.2)	22.1	(1.9)	4.3	(1.4)	1.3	(0.5)	2.0	(1.0)	4.6	(2.3)	2.9	(0.2)	3.7	(0.9)	101	160	(33)	8.7	(0.2)
AJ99 Basanite	1175	24.5	0.39	0.61	-1.1	-16.7	48.0	(1.3)	2.6	(0.2)	16.2	(1.4)	10.6	(1.3)	-	-	6.3	(0.5)	10.5	(1.5)	2.3	(1.0)	0.30	(0.41)	97	1333	(60)	9.1	(0.2)
Fe-free T-Phonolite	1175	24.5	0.39	0.61	-1.1	-16.7	55.8	(1.6)	2.3	(0.2)	22.2	(0.9)	4.6	(1.0)	1.1	(0.3)	2.3	(1.1)	3.4	(2.4)	3.0	(0.3)	4.4	(0.9)	99	446	(51)	8.6	(0.2)
Foidite	1175	24.5	0.39	0.61	-1.1	-16.7	53.5	(1.4)	2.7	(0.6)	25.3	(0.9)	2.2	(0.8)	0.14	(0.05)	0.17	(0.07)	0.31	(0.08)	9.8	(0.5)	6.1	(0.3)	100	653	(110)	8.8	(0.2)
Phonolite	1175	24.5	0.39	0.61	-1.1	-16.7	60.2	(1.4)	1.5	(0.2)	16.0	(1.6)	3.4	(0.3)	1.4	(0.2)	3.1	(0.4)	5.4	(1.0)	4.0	(0.2)	2.9	(0.4)	98	1708	(214)	9.2	(0.2)
T-Andesite	1175	24.5	0.39	0.61	-1.1	-16.7	57.2	(1.1)	3.8	(0.7)	25.0	(1.3)	2.0	(0.5)	0.33	0.17	0.26	(0.11)	0.92	(0.26)	4.2	(0.5)	6.1	(0.3)	100	95	(48)	8.0	(0.3)
T-Basaltic Andesite	1175	24.5	0.39	0.61	-1.1	-16.7	56.0	(2.0)	2.3	(0.6)	22.3	(1.0)	3.3	(1.3)	1.1	(0.2)	1.9	(0.9)	5.0	(1.8)	2.9	(0.5)	3.7	(0.8)	99	82	(26)	7.9	(0.2)
AJ99 Basanite	1193	15.5	0.38	0.62	-1.1	-16.4	48.2	(0.4)	2.5	(0.1)	15.8	(0.7)	8.8	(0.5)	0.37	(0.06)	6.2	(1.0)	11.0	(0.3)	3.2	(0.2)	1.0	(0.1)	97	1702	(195)	9.1	(0.2)
High-Mg Basalt	1193	15.5	0.38	0.62	-1.1	-16.4	45.3	(0.3)	4.2	(0.2)	10.8	(0.4)	10.3	(0.4)	0.19	(0.01)	11.8	(2.1)	12.5	(0.5)	1.5	(0.1)	0.31	(0.02)	97	2411	(174)	9.2	(0.2)
Icelandic Basalt	1193	15.5	0.38	0.62	-1.1	-16.4	49.6	(0.3)	1.0	(0.0)	14.4	(0.1)	8.7	(0.2)	0.18	(0.02)	8.5	(0.1)	11.9	(0.1)	2.5	(0.1)	1.0	(0.0)	98	2239	(105)	9.2	(0.2)
Nephelenite	1193	15.5	0.38	0.62	-1.1	-16.4	43.6	(0.2)	2.8	(0.0)	14.5	(0.1)	8.3	(0.1)	2.32	(0.05)	7.5	(0.1)	14.3	(0.1)	3.1	(0.1)	0.77	(0.02)	98	4551	(239)	9.5	(0.2)
Nepheline Basanite	1193	15.5	0.38	0.62	-1.1	-16.4	47.9	(0.3)	2.5	(0.0)	12.1	(0.1)	9.4	(0.1)	0.19	(0.02)	10.2	(0.1)	10.4	(0.1)	2.9	(0.1)	0.76	(0.02)	97	2406	(286)	9.2	(0.2)
T-Basalt	1193	15.5	0.38	0.62	-1.1	-16.4	48.3	(0.3)	2.4	(0.0)	16.7	(0.1)	8.5	(0.1)	0.38	(0.02)	5.0	(0.0)	11.3	(0.0)	3.1	(0.1)	1.1	(0.0)	97	1765	(198)	9.1	(0.2)
T-Phonolite	1193	15.5	0.38	0.62	-1.1	-16.4	56.0	(0.3)	1.6	(0.0)	21.7	(0.2)	5.1	(0.1)	0.14	(0.02)	2.0	(0.0)	4.4	(0.1)	7.2	(0.2)	2.7	(0.1)	101	712	(70)	8.7	(0.2)
AJ99 Basanite	1223	24	0.39	0.61	-1.1	-15.9	47.1	(0.6)	3.1	(0.1)	15.4	(0.2)	10.6	(0.1)	-	-	6.4	(0.1)	10.7	(0.1)	2.7	(0.1)	0.61	(0.03)	97	1047	(115)	8.6	(0.2)
Fe-free T-Phonolite	1223	24	0.39	0.61	-1.1	-15.9	59.9	(1.1)	1.8	(0.2)	22.2	(0.8)	0.07	(0.01)	0.13	(0.02)	2.1	(0.3)	5.3	(0.8)	5.8	(0.2)	2.1	(0.2)	99	402	(65)	8.2	(0.2)
Foidite	1223	24	0.39	0.61	-1.1	-15.9	56.4	(1.3)	2.7	(0.2)	25.2	(0.4)	2.8	(0.3)	0.21	(0.03)	0.26	(0.03)	2.2	(0.1)	7.6	(0.5)	2.4	(0.1)	100	544	(146)	8.3	(0.2)
High-Mg Basalt	1223	24	0.39	0.61	-1.1	-15.9	44.2	(0.2)	4.1	(0.0)	15.0	(0.2)	9.3	(0.1)	0.17	(0.02)	10.6	(0.2)	11.3	(0.1)	1.4	(0.1)	0.28	(0.01)	97	1137	(57)	8.6	(0.2)
Phonolite	1223	24	0.39	0.61	-1.1	-15.9	43.5	(0.3)	4.1	(0.0)	14.3	(0.1)	9.3	(0.1)	0.18	(0.02)	10.9	(0.0)	11.4	(0.1)	1.3	(0.1)	0.29	(0.01)	95	1120	(51)	8.6	(0.2)
T-Andesite	1223	24	0.39	0.61	-1.1	-15.9	57.3	(2.6)	3.2	(0.6)	23.9	(2.6)	2.3	(0.9)	0.22	(0.09)	0.25	(0.10)	1.9	(0.7)	4.7	(0.6)	4.9	(0.2)	100	147	(23)	7.7	(0.2)
T-Basalt	1223	24	0.39	0.61	-1.1	-15.9	44.8	(0.5)	2.5	(0.0)	16.5	(0.1)	10.5	(0.1)	0.32	(0.02)	4.3	(0.0)	11.8	(0.1)	3.1	(0.1)	1.0	(0.0)	95	1364	(50)	8.7	(0.2)
T-Basaltic Andesite	1223	24	0.39	0.61	-1.1	-15.9	55.8	(1.5)	2.2	(0.2)	22.0	(1.6)	4.1	(0.4)	1.1	(0.1)	2.0	(0.3)	4.9	(1.8)	3.5	(0.5)	3.3	(0.6)	99	140	(35)	7.7	(0.2)